Neurosci. **30,** 220–227
5. Tye, K. M., Tye, L. D., Cone, J. J., Hekkelman, E. F., Janak, P. H., and Bonci, A. (2010) *Nat. Neurosci.* **13,** 475–481
6. Simpson, E. H., Kellendonk, C., Kandel, E. (2010) *Neuron* **65,** 585–596
7. Bernheimer, H., Birkmayer, W., Hornykiewicz, O., Jellinger, K., Seitelberger, F. (1973) *J. Neurol. Sci.* **20,** 415–455
8. Bezard, E., Gross, C. E., and Brotchie, J. M. (2003) *Trends Neurosci.* **26,** 215–221
9. McCallum, S. E., Parameswaran, N., Perez, X. A., Bao, S., McIntosh, J. M., Grady, S. R., and Quik, M. (2006) *J. Neurochem.* **96,** 960–972
10. Pifl, C., and Hornykiewicz, O. (2006) *Neurochem. Int.* **49,** 519–524
11. Perez, X. A., Parameswaran, N., Huang, L. Z., O'Leary, K. T., and Quik, M. (2008) *J. Neurochem.* **105,** 1861–1872
12. Kobayashi, K., Morita, S., Sawada, H., Mizuguchi, T., Yamada, K., Nagatsu, I., Hata, T., Watanabe, Y., Fujita, K., and Nagatsu, T. (1995) *J. Biol. Chem.* **270,** 27235–27243
13. Thomas, S. A., Matsumoto, A. M., and Palmiter, R. D. (1995) *Nature* **374,** 643–646
14. Zhou, Q. Y., Quaife, C. J., Palmiter, R. D. (1995) *Nature* **374,** 640–643
15. Zhou, Q. Y., and Palmiter, R. D. (1995) *Cell* **83,** 1197–1209
16. Szczypka, M. S., Kwok, K., Brot, M. D., Marck, B. T., Matsumoto, A. M., Donahue, B. A., and Palmiter, R. D. (2001) *Neuron* **30,** 819–828
17. Hnasko, T. S., Perez, F. A., Scouras, A. D., Stoll, E. A., Gale, S. D., Luquet, S., Phillips, P. E, Kremer, E. J., and Palmiter, R. D. (2006) *Proc. Natl. Acad. Sci. U.S.A.* **103,** 8858–8863
18. Nagatsu, T., Levitt, M., and Udenfriend, S. (1964) *J. Biol. Chem.* **239,** 2910–2917
19. Li, X. G., Okada, T., Kodera, M., Nara, Y., Takino, N., Muramatsu, C., Ikeguchi, K., Urano, F., Ichinose, H., Metzger, D., Chambon, P., Nakano, I., Ozawa, K., and Muramatsu, S. (2006) *Mol. Ther.* **13,** 160–166
20. Kadkhodaei, B., Ito, T., Joodmardi, E., Mattsson, B., Rouillard, C., Carta, M., Muramatsu, S., Sumi-Ichinose, C., Nomura, T., Metzger, D., Chambon, P., Lindqvist, E., Larsson, N. G., Olson, L., Björklund, A., Ichinose, H., and Perlmann, T. (2009) *J. Neurosci.* **16,** 15923–15932
21. Dittgen, T., Nimmerjahn, A., Komai, S., Licznerski, P., Waters, J., Margrie, T. W., Helmchen, F., Denk, W., Brecht, M., and Osten, P. (2004) *Proc. Natl. Acad. Sci. U.S.A.* **101,** 18206–18211
22. Paxinos, G., and Franklin, K. B. (2004) *The Mouse Brain in Stereotaxic Coordinates,* Academic Press, Inc., San Diego, CA
23. Prensa, L., and Parent, A. (2001) *J. Neurosci.* **21,** 7247–7260
24. Matsuda, W., Furuta, T., Nakamura, K. C., Hioki, H., Fujiyama, F., Arai, R., and Kaneko, T. (2009) *J. Neurosci.* **29,** 444–453
25. Ungerstedt, U., and Arbuthnott, G. W. (1970) *Brain Res.* **24,** 485–493
26. Lane, E. L., Cheetham, S., and Jenner, P. (2005) *J. Pharmacol. Exp. Ther.* **312,** 1124–1131
27. Dunkley, P. R., Bobrovskaya, L., Graham, M. E., von Nagy-Felsobuki, E. I., and Dickson, P. W. (2004) *J. Neurochem.* **91,** 1025–1043
28. Tank, A. W., Curella, P., and Ham, L. (1986) *Mol. Pharmacol.* **30,** 497–503
29. Fernández, E., and Craviso, G. L. (1999) *J. Neurochem.* **73,** 169–178
30. Lin, A. C., and Holt, C. E. (2008) *Curr. Opin. Neurobiol.* **18,** 60–68
31. Willis, D. E., and Twiss, J. L. (2006) *Curr. Opin. Neurobiol.* **16,** 111–118
32. Jarrott, B., and Geffen, L. B. (1972) *Proc. Natl. Acad. Sci. U.S.A.* **69,** 3440–3442
33. Terada, S. (2003) *Neurosci. Res.* **47,** 367–372
34. Hirokawa, N., Niwa, S., and Tanaka, Y. (2010) *Neuron* **68,** 610–638
35. Zigmond, M. J., Acheson, A. L., Stachowiak, M. K., and Stricker, E. M. (1984) *Arch. Neurol.* **41,** 856–861
36. Cubeddu, L. X., and Hoffmann, I. S. (1982) *J. Pharmacol. Exp. Ther.* **223,** 497–501
37. Håkansson, K., Pozzi, L., Usiello, A., Haycock, J., Borrelli, E., and Fisone, G. (2004) *Eur. J. Neurosci.* **20,** 1108–1112
38. Rice, M. E., and Cragg, S. J. (2008) *Brain Res. Rev.* **58,** 303–313
39. Mosharov, E. V., Larsen, K. E., Kanter, E., Phillips, K. A., Wilson, K., Schmitz, Y., Krantz, D. E., Kobayashi, K., Edwards, R. H., and Sulzer, D. (2009) *Neuron* **62,** 218–229
40. Gordon, S. L., Quinsey, N. S., Dunkley, P. R., and Dickson, P. W. (2008) *J. Neurochem.* **106,** 1614–1623
41. Pothos, E. N., Davila, V., and Sulzer, D. (1998) *J. Neurosci.* **18,** 4106–4118
42. Hefti, F., Enz, A., and Melamed, E. (1985) *Neuropharmacology* **24,** 19–23
43. Fukushima, T., and Nixon, J. C. (1980) Anal. Biochem. **102,** 176–188

SYNAPSE 63:541–548 (2009)

Multitracer Assessment of Dopamine Function After Transplantation of Embryonic Stem Cell-Derived Neural Stem Cells in a Primate Model of Parkinson's Disease

SHIN-ICHI MURAMATSU,[1]* TSUYOSHI OKUNO,[2] YUTAKA SUZUKI,[2] TAKASHI NAKAYAMA,[3] TAKEHARU KAKIUCHI,[4] NAOMI TAKINO,[1] ASAKO IIDA,[1] FUMIKO ONO,[5] KEIJI TERAO,[5] NOBUO INOUE,[6] IMAHARU NAKANO,[1] YASUSHI KONDO,[2] AND HIDEO TSUKADA[4]

[1]*Divison of Neurology, Department of Medicine, Jichi Medical University, Tochigi 329-0498, Japan*
[2]*Mitsubishi Tanabe Pharma Corporation, Osaka 532-8505, Japan*
[3]*Department of Biochemistry I, Yokohama City University School of Medicine, Kanagawa 236-0004, Japan*
[4]*Central Research Laboratory, Hamamatsu Photonics K.K., Shizuoka 434-8601, Japan*
[5]*Tsukuba Primate Research Center, National Institute of Biomedical Innovation, Ibaraki 305-0843, Japan*
[6]*Division of Regenerative Neurosciences, Tokyo Metropolitan University, Tokyo 116-8551, Japan*

KEY WORDS ES cell; PET; monkey; MPTP

ABSTRACT The ability of primate embryonic stem (ES) cells to differentiate into dopamine (DA)-synthesizing neurons has raised hopes of creating novel cell therapies for Parkinson's disease (PD). As the primary purpose of cell transplantation in PD is restoration of dopaminergic neurotransmission in the striatum, in vivo assessment of DA function after grafting is necessary to achieve better therapeutic effects. A chronic model of PD was produced in two cynomolgus monkeys (M-1 and M-2) by systemic administration of neurotoxin. Neural stem cells (NSCs) derived from cynomolgus ES cells were implanted unilaterally in the putamen. To evaluate DA-specific functions, we used multiple [^{11}C]-labeled positron emission tomography (PET) tracers, including [β-^{11}C]L-3,4-dihydroxyphenylalanine (L-[β-^{11}C]DOPA, DA precursor ligand), [^{11}C]-2β-carbomethoxy-3β-(4-fluorophenyl)tropane ([^{11}C]β-CFT, DA transporter ligand) and [^{11}C]raclopride (D_2 receptor ligand). At 12 weeks after grafting NSCs, PET demonstrated significantly increased uptake of L-[β-^{11}C]DOPA (M-1:41%, M-2:61%) and [^{11}C]β-CFT (M-1:31%, M-2:36%) uptake in the grafted putamen. In addition, methamphetamine challenge in M-2 induced reduced [^{11}C]raclopride binding (16%) in the transplanted putamen, suggesting release of DA. These results show that transplantation of NSCs derived from cynomolgus monkey ES cells can restore DA function in the putamen of a primate model of PD. PET with multitracers is useful for functional studies in developing cell-based therapies against PD. **Synapse 63:541–548, 2009.** ©2009 Wiley-Liss, Inc.

INTRODUCTION

In Parkinson's disease (PD), the cardinal symptoms such as rest tremor, muscular rigidity and bradykinesia, become apparent after 40–50% of the neurons in the substantia nigra pars compacta (SNc) have been lost and striatal dopamine (DA) has been reduced to about 20% of normal levels (Kish et al., 1988). As a treatment for advanced PD, neural transplantation has been investigated for more than two decades with the aim of replacing degenerated DA neurons and restoring dopaminergic neurotransmission in the striatum. Embryonic stem (ES) cells may offer a substitute for currently used fetal midbrain cells, because they can proliferate extensively in an undifferentiated state and may provide an unlimited source of DA neurons (Li et al., 2008; Newman and Bakay, 2008). Transplantation of DA neurons derived from mouse ES cells

Contract grant sponsors: Ministry of Health, Labor and Welfare of Japan, Ministry of Education, Culture, Sports, Science and Technology of Japan (Special Coordination Funds), Japan Society for the Promotion of Science (Grant-in-Aid for Creative Scientific Research), CREST, the Japan Science and Technology Agency (JST).

*Correspondence to: Shin-Ichi Muramatsu, Division of Neurology, Department of Medicine, Jichi Medical University, 3311-1 Yakushiji, Shimotsuke, Tochigi 329-0498, Japan. E-mail: muramats@ms.jichi.ac.jp

Received 18 August 2008; Accepted 31 October 2008

DOI 10.1002/syn.20634

Published online in Wiley InterScience (www.interscience.wiley.com).

showed electrophysiological and behavioral properties expected of neurons from the midbrain in a rat model of PD (Chung et al., 2006; Kim et al., 2002; Rodriguez-Gomez et al., 2007). Survival of DA neurons obtained in vitro from primate ES cells was also reported in primate hosts (Sanchez-Pernaute et al., 2005; Takagi et al., 2005), but the dopaminergic function of these cells in the primate brain has not been fully evaluated.

Positron emission tomography (PET) is a valuable method for imaging altered DA function in PD. The most common tracer used to visualize and assess the integrity of DA presynaptic systems is 6-[^{18}F]fluoro-L-4-dihydroxyphenylalanine ([^{18}F]FDOPA), a fluoro-analog of 4-dihydroxyphenylalanine (L-dopa). However, uptake of this agent is increased in variable conditions such as inflammation and tumor formation, and assessment of graft function using only this ligand is difficult. The present study therefore used PET with multitracers to analyze both presynaptic and postsynaptic dopaminergic functions and found that transplantation of neural stem cells (NSCs) induced from primate ES cells restored DA function in a primate model of PD.

MATERIALS AND METHODS

Cell culture and differentiation

Astrocyte-conditioned medium (ACM) was prepared by culturing astrocytes obtained from mouse fetal cerebra (Inoue et al., 1988) in DMEM/F12 medium (Invitrogen, Carlsbad, CA) containing N2 supplement (Invitrogen). The CMK6 cynomolgus monkey ES cell line (Suemori et al., 2001) was seeded at a clonal density and grown on a mitomycin C-treated mouse embryonic fibroblast feeder layer in DMEM/F12 medium (Invitrogen) supplemented with 1000 U/ml leukemia inhibitory factor (Chemicon, Temecula, CA), 1 mM β-mercaptoethanol (Invitrogen), and 15% knockout serum replacement (Invitrogen). Colonies of undifferentiated ES cells with a diameter of 300–500 μm and grown for 7–9 days were treated with 0.1% collagenase for 5 min and then detached whole using a glass capillary. Colonies were transferred to nonadhesive bacteriological dishes in ACM supplemented with 20 ng/ml of recombinant human fibroblast growth factor (FGF)-2 (R&D Systems, Minneapolis, MN) and 20 ng/ml of recombinant epidermal growth factor (EGF) (R&D Systems). Colonies were cultured for 10 days, giving rise to floating spheres comprising numerous NSCs. To stimulate proliferation, these spheres were plated onto Matrigel-coated dishes and cultivated for up to 10 days in Neurobasal medium (Invitrogen) supplemented with 2% B-27 (Invitrogen), 20 ng/ml of FGF-2, and 20 ng/ml of EGF. To efficiently induce DA-synthesizing neurons, the medium was replaced with ACM supplemented with 50 ng/ml of sonic hedgehog (Shh; R&D Systems) 1 day before transplantation.

Animals and neurotoxin treatment

All experiments were performed in full compliance with the requirements of the institutional animal care and use committee. Two cynomolgus monkeys (*Macaca fascicularis*), M-1 and M-2, weighing 2.3–2.5 kg were used for the cell therapy experiments. The monkeys were housed under standard conditions of humidity and dark/light cycles with ad libitum access to food and water. To create bilateral striatal lesions, 1-methyl-4-phenyl-1,2,3,6-tetrahydropyridine (MPTP, 0.2–0.4 mg/kg of free base; Sigma-Aldrich Japan K.K., Tokyo, Japan) in phosphate-buffered saline (PBS) was injected intravenously once per week over a 4-month period until a stable parkinsonian syndrome was observed. The total dose of MPTP administered was 1.5 and 2.95 mg/kg. To avoid the possibility of spontaneous recovery from the effects of MPTP, which could mimic the behavioral effect of cell transplantation, the monkeys were allowed to recover for 2 months after the last MPTP treatment.

Transplantation procedures

All surgical procedures were performed in an aseptic environment with the monkeys under isoflurane (1–2%) anesthesia. The head was placed in a stereotaxic device (Kopf Instruments, Tujunga, CA). Each monkey received nine injections of NSCs derived from cynomolgus monkey ES cells (M-1, 1×10^5 viable cells; M-2, 2×10^7 viable cells) in three tracts in the left putamen. NSCs were trypsinized and resuspended in 72 μl of ACM supplemented with Shh. Eight microliters of NSC suspension was injected into each of the nine points using a 50-μl Hamilton microsyringe fitted with a 26-gauge needle over a period of 5 min. The needle was left in place for an additional 3 min to prevent the loss of cells by backflow. As a control, 25 μl of ACM supplemented with Shh was injected into the right putamen. Stereotaxic coordinates of injection sites in the putamen were: Track 1, anterior 13.4 mm, lateral 12 mm, depth +19, 17, 15 mm from the midpoint of the ear bar; Track 2, anterior 16.4 mm, lateral 11.5 mm, depth +20, 18, 16 mm; and Track 3, anterior 18.1 mm, lateral 11 mm, depth +19, 17, 15 mm. From 3 days before surgery, the monkeys received daily intramuscular injections of 0.5 mg/kg of the immunosuppressant FK506 (Astellas Pharmaceuticals, Osaka, Japan) diluted in physiological saline. From 5 days after surgery, the dose was reduced to 0.2 mg/kg for the rest of the experimental period.

PET

Magnetic resonance imaging (MRI) of both monkeys was performed at the National Institute for Physiological Sciences using a 3.0-T imager (Allegra; Sie-

mens, Erlangen, Germany) under pentobarbital anesthesia. Stereotaxic coordinates of PET and MRI were adjusted based on the orbitomeatal (OM) plane with a specially designed head holder. Syntheses of [^{11}C]-labeled-compounds have been described (Tsukada et al., 2000a,b). Data were collected on a high-resolution animal PET scanner (SHR-7700; Hamamatsu Photonics, Hamamatsu, Japan) with a transaxial resolution of 2.6 mm full-width at half-maximum and a center-to-center distance of 3.6 mm (Watanabe et al., 1997). The PET camera allowed 31 slices to be recorded simultaneously. After fasting overnight, the monkey under isoflurane anesthesia was secured to a monkey head folder with stereotaxic coordinates aligned parallel to the OM plane. Each of the [^{11}C]-labeled compounds was delivered through a posterior tibial vein cannula. PET with [^{11}C]L-3,4-dihydroxyphenylalanine (L-[β-^{11}C]DOPA), the precursor of DA synthesis, and [^{11}C]raclopride, a reversible D_2 receptor antagonist, were performed for a total of 64 min with 6 time frames at 10 sec intervals and 12 time frames at 1 min, followed by 16 time frames at 3 min. PET with [^{11}C]2β-carbomethoxy-3β-(4-fluorophenyl)-tropane ([^{11}C]β-CFT) was performed with an additional 19 time frames at 3 min for a total of 91 min. To measure DA release in the striatum indirectly in vivo as reflected by reductions in DA receptor availability, [^{11}C]raclopride was injected through the cannula 30 min after administration of either 0.5 mg/kg of amphetamine or saline. Time-activity curves of each labeled compound in regions of interest chosen from magnetic resonance images were obtained.

For quantification of in vivo binding of [^{11}C]raclopride and [^{11}C]β-CFT, a kinetic 3-compartment analysis method was applied as previously described (Huang et al., 1986). The time-activity curves of plasma and of each region were fitted to a 3-compartment model using the least-squares method. Binding potentials of [^{11}C]raclopride and [^{11}C]β-CFT were calculated by determining the ratio of the estimated k_3 value (association rate) to the estimated k_4 value (dissociation rate). For quantification of L-[β-^{11}C]DOPA utilization rate constant in the striatum of the monkey brain, a graphical analysis method was applied to calculate DA synthesis rate (k_3) as described previously (Tsukada et al., 2000a,b).

Behavioral assessment

Animals were clinically evaluated twice a week using a primate parkinsonism rating scale (PPRS) and activities were recorded on digital videotape. The PPRS is based on the Unified Parkinson's Disease Rating Scale, but was developed specifically for nonhuman primates (Jenner, 2000). On PPRS, scores from 0 (normal) to 4 (maximal disability) are given for each of the six following parkinsonian features: spatial hypokinesia in movements around the cage, bradykinesia, manual dexterity of the right arm, manual dexterity of the left arm, balance, and freezing.

Immunocyto- and immunohistochemistry

Cells cultured on coverslips were fixed with 4% paraformaldehyde in 0.1 M PBS (pH 7.2) for 20 min at 4°C. Cells were then treated with 10% normal horse serum, 2% bovine albumin, and 0.2% Triton X-100 in 0.1 M PBS (pH 7.2) for 20 min at room temperature and incubated further in the presence of the following antibodies separately: nestin (1:200, Chemicon); high-molecular-mass neurofilament protein (NF-H) (1:500, Chemicon); glial fibrillary acidic protein (GFAP) (1:200, Chemicon); O4 (1:200, Chemicon); tyrosine hydroxylase (TH) (1:500, Chemicon); aromatic L-amino acid decarboxylase (AADC) (1:200, Sigma); DA transporter (DAT) (1:200, Chemicon); choline acetyl transferase (ChAT) (1:500 Chemicon); serotonin (5HT) (1:1000, Sigma); and glutamic acid decarboxylase (GAD) (1:1000, Sigma). Cells were washed and then incubated in Alexa Fluor 488- and Alexa Fluor 594-labeled secondary antibodies (1:200; Molecular Probes, Eugene, OR). Cells were mounted in Vectashield containing 4,6-diamidino-2-phenylindole (DAPI; Vector Laboratories, Burlingame, CA) and analyzed under a fluorescence microscope (Eclipse E800; Nikon, Tokyo, Japan) equipped with phase-contrast optics or under a confocal laser-scanning microscope (LSM 510; Carl Zeiss Microimaging Co., Tokyo, Japan). Quantitative immunocytochemical data obtained from 4 to 9 cultures are expressed as mean ± standard error of the mean.

Under deep anesthesia, monkeys were perfused with 4% paraformaldehyde through the ascending aorta. The brains were removed and cut into several blocks 5-mm thick. These blocks were postfixed in the same fixative, left for 3 days in PBS containing 30% sucrose, and then cut on a cryostat into coronal sections 30-μm thick. Sections were treated with 0.3% H_2O_2 for 15 min to inhibit endogenous peroxidase. Sections were incubated at 4°C for 2 days in PBS containing 0.3% Triton X-100 and primary antibodies against mouse monoclonal anti-TH antibody (1:8000; Immnostar, Hudson, WI). Next, sections were incubated in biotinylated antimouse immunoglobulin (Ig)G (1:1000; Vector Laboratories) for 1 h at room temperature, and finally in avidin-biotin-peroxidase complex (1:50; Vector Laboratories) for 30 min at room temperature. Peroxidase activity was revealed in 50 mM Tris-HCl buffer (pH 7.6) containing 0.0004% H_2O_2 and 0.01% 3,3′-diaminobenzidine-4HCl (DAB) (all from Vector Laboratories). For immunofluorescence staining, sections were incubated with mouse monoclonal anti-TH antibody (1:800; Immnostar), rabbit anti-5HT antibody (1:2500; Incstar,

Stillwater, MN), or anti-Ki 67 antibody (1:200; Chemicon) followed by incubation with Alexa Fluor 594-conjugated goat antimouse IgG (1:1000; Molecular Probes). Immunoreactivity was assessed and viewed under confocal laser scanning microscopy (TCS NT; Leica Microsystems, Tokyo, Japan). We estimated TH-immunoreactive (IR) cell counts in serial sections (every 10th) under ×63 magnification on a Zeiss microscope equipped with a video camera.

RESULTS

Efficient induction of DA neurons in culture

A colony of undifferentiated ES cells formed spheres with unique concentric stratiform structure when cultivated in ACM supplemented with FGF-2 and EGF under free-floating conditions, as reported previously (Nakayama et al., 2003, 2004). These spheres displayed peripheral NSCs with a center of proliferating ES cells. Subsequent culture on an adhesive substrate formed circular clusters of cells from which many nestin-positive NSCs migrated. After a few passages, almost all cells expressed nestin (99.5% ± 0.5%) and only a few cells (<0.5%) expressed NF-H. To examine differentiation properties in vitro, a small fraction of NSCs were grown in ACM with Shh. After 5 days, cells in culture displayed a neuronal appearance with long neuritis and became positive for NF-H (99.5% ± 0.5%). Cells were immunoreactive for neither antibody against the astrocyte marker GFAP nor the antibody against oligodendrocyte protein O4 (data not shown). Moreover, many (70% ± 1%) NF-H-positive cells expressed DA neuronal markers such as TH, AADC, and DAT (Fig. 1). Small proportions of NF-H-positive cells expressed either 5HT (12.2% ± 1.3%), ChAT (1.0% ± 0.6%), or GAD (11.9% ± 1.6%).

DA production is restored in the grafted putamen

We used PET to assess nigrostriatal dopaminergic function in MPTP-treated monkeys before and after NSC implantation. MPTP-intoxicated monkeys displayed comprehensive loss of uptake for L-[β-^{11}C]DOPA, a substrate for AADC, and [^{11}C]β-CFT, a DA transporter ligand, in both hemispheres of the brain before transplantation, suggesting severe loss of DA terminals (Figs. 2A and 2B). At 4 weeks postoperatively, we found increases in both L-[β-^{11}C]DOPA and [^{11}C]β-CFT uptake in the grafted putamen. Quantitative analysis of scans at 4 weeks after implantation revealed significant increases in both L-[β-^{11}C]DOPA uptake (M-1, 41%; M-2, 61%) and [^{11}C]β-CFT uptake (M-1, 33%; M-2, 36%) in the implanted striatum compared with the control putamen (Figs. 2C and 2D). The degree of decrease in striatal radioactivity from [^{11}C]raclopride after amphetamine challenge in M-2 was significantly higher in the grafted putamen (16%) than in the control putamen (0.6%), indicating increased release of DA in the striatum (Fig. 3).

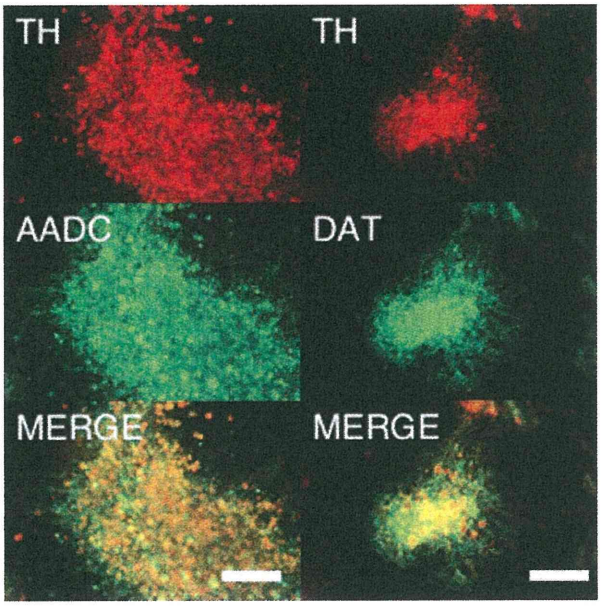

Fig. 1. Neurons derived from ES cells show markers of DA-synthesizing cells. Dual labeling with antityrosine hydroxylase (TH) and antiaromatic L-amino acid decarboxylase (AADC) antibodies shows coexpression of dopamine (DA)-synthesizing enzymes in the neurons. Dual labeling with anti-TH and anti-DA transporter (DAT) antibodies indicates the DA phenotype. Scale bar: 50 μm.

Behavioral recovery is modest

After chronic administration of MPTP, monkeys developed bilateral parkinsonism manifested by a loss of spontaneous motor activity, bradykinesia, impairment of manual dexterity, tremor, and freezing. Parkinsonian features were stable for 2 months from the last MPTP treatment. Three months after unilateral cell transplantation into the putamen, both monkeys showed modest behavioral improvements demonstrated by both PPRS and systematic analysis of digital videotapes. Before MPTP treatment, both monkeys scored 0 on PPRS. After MPTP, but before implantation, mean scores of four evaluations on the PPRS were 14 for M-1 and 12 for M-2. At 12 weeks after implantation, this score reduced to 11 and 10, respectively. In M-2, the score remained constant during the observation period until 6 months after implantation. Regardless of on- or off-medication, no dyskinesia was observed.

Grafted cells differentiate into TH-positive cells in the brain

Histological assessment of brains was performed for M-1 and M-2 at 3 and 6 months after implantation,

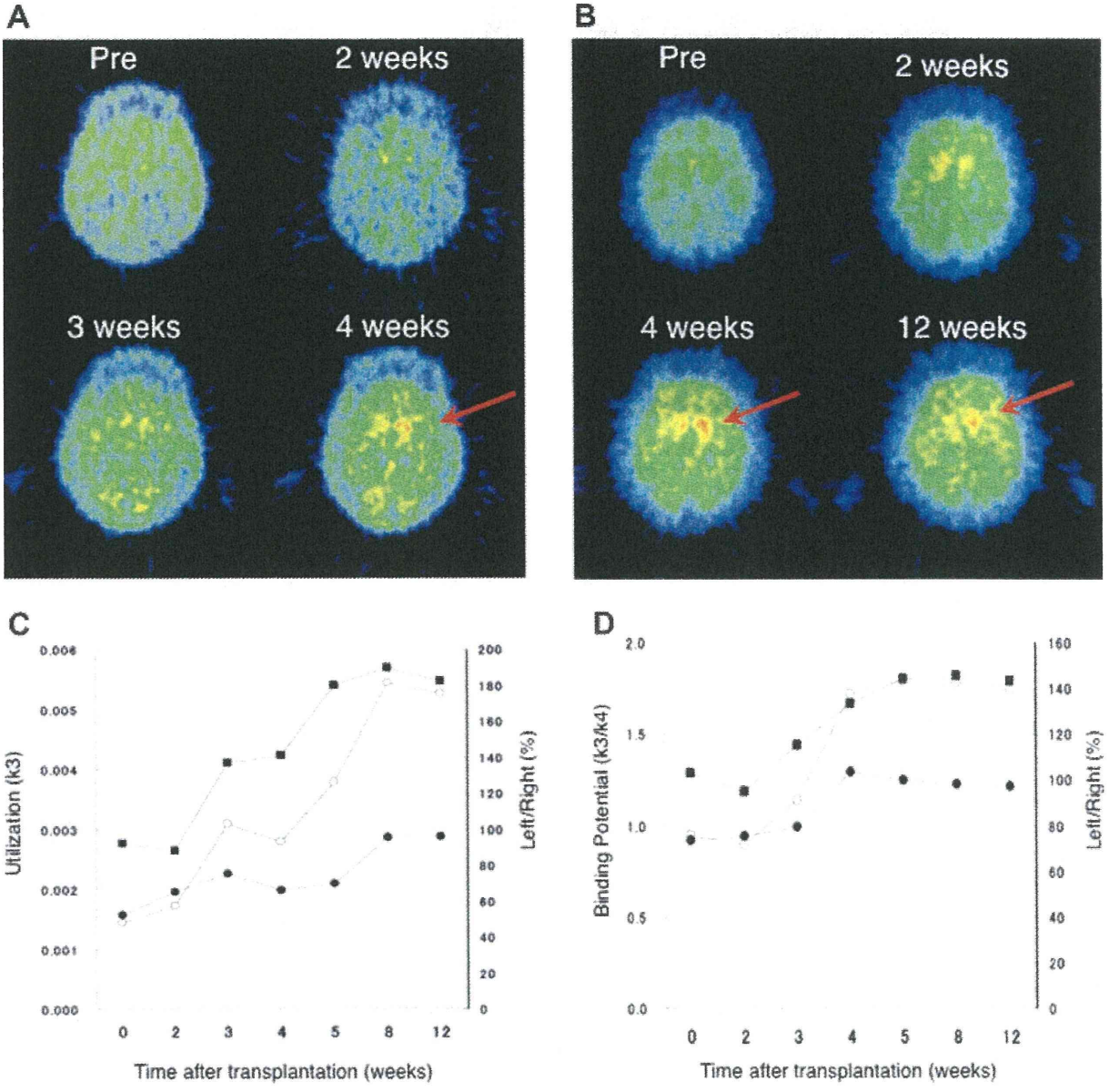

Fig. 2. (**A**, **B**) PET images of L-[β-^{11}C]DOPA (A) and [^{11}C]β-CFT (B) uptake in monkey M-1 before and after cell transplantation. Four weeks after implantation, increased radionuclide uptake was detected in the implanted putamen (arrows). (**C**, **D**) Graphic representation of relative changes in signal strength over time in the same animal, showing significant increases in L-[β-^{11}C]DOPA utilization (k_3 value) (C) and [^{11}C]β-CFT binding potential (BP) (k_3/k_4 value) (D) in the implanted (left: open circles) putamen compared with control (right: filled circles) putamen. Filled squares indicate left to right ratio.

respectively. Many TH-IR cells, about 1000 in M-1 and 3000 in M-2, thrived in the grafted putamen (Fig. 4). Less than 50 TH-IR cells were found in the putamen on the side contralateral to the graft. A small number of 5HT-IR cells was identified in the grafted putamen (<5 cells). No TH-positive cells were positive for the proliferation marker Ki-67. Hematoxylin and eosin staining showed no signs of teratoma-like structures in the transplanted putamen.

DISCUSSION

This study demonstrated with PET that engraftment of NSCs derived from primate ES cells has the capacity to restore DA function in a primate model of PD. Transplantation of neural precursors has become one of the key strategies for cell replacement in the brain. To bypass the shortage of donor tissue, a wide range of experimental approaches have been studied, including proliferation of NSCs in vitro stimulated by

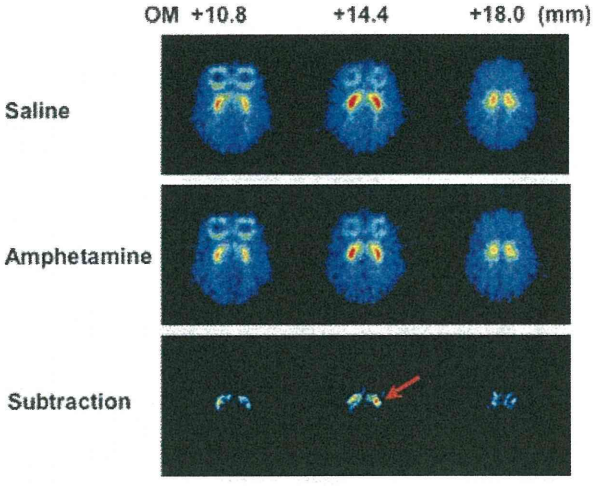

Fig. 3. Drug-induced release of DA in the grafted striatum 12 weeks after transplantation in monkey M-2. After methamphetamine administration, [^{11}C]raclopride binding in the implanted putamen was significantly reduced compared with that in the control putamen. Each slice image after methamphetamine infusion (middle row) was subtracted from a corresponding baseline image (upper row). Subtraction images (lower row). The images of each column are in horizontal plane and same stereotaxic coordinates (mm) from the orbitomeatal (OM) line. Arrows indicate the side of the implant.

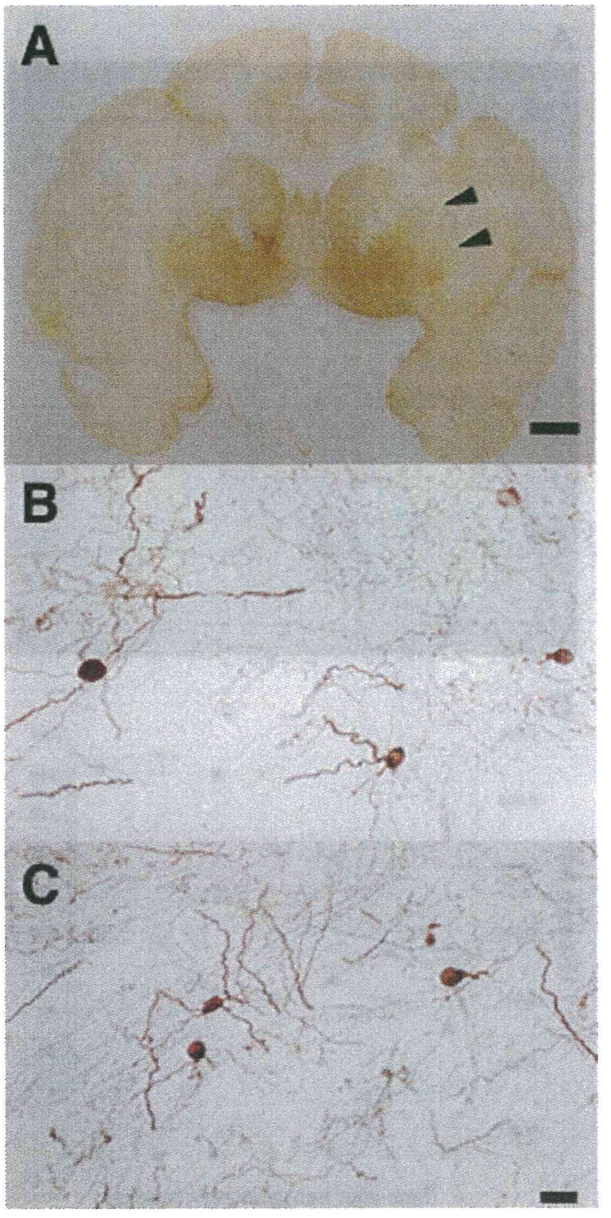

Fig. 4. TH-IR cells in the unilateral putamen of monkey M-1 at 3 months after cell implantation. (**A**) Restoration of TH-IR in the implanted putamen (arrowhead) is not obvious at low magnification. However, TH-IR neurons are apparent in dorsal (**B**) and ventral (**C**) portions of the implanted putamen. Scale bar: 0.5 cm (A); 20 μm (B, C).

mitogen treatment, ex vivo introduction of growth stimulating oncogenes, xenotransplantation, enhancement of endogenous adult neurogenesis, and attempts to recruit non-neural adult stem cells from other tissues (Hall et al., 2007; Liu, 2008). However, in addition to the limited plasticity and slow propagation of adult stem cells, continuous expression of oncogenes or stimulation of mitogens raises question about the long-term safety of these strategies. Of the various candidate donor cells, ES cells are the most attractive due to the characteristics of pluripotency and the potential for unlimited self-renewal. Although human ES cells seem promising for clinical applications, an alternative model system based on ES cells derived from nonhuman primates is necessary for preclinical studies, including allogenic transplantation.

The present study used cynomolgus monkey ES cells that resemble human ES cells but are distinct from murine ES cells in terms of morphology, expression of surface markers and feeder- and leukemia inhibitory factor-dependence, among other factors (Suemori et al., 2001). We have previously shown that astrocyte-derived factors instruct mouse and primate ES cells to differentiate into neurons quickly and efficiently (Nakayama et al., 2003, 2004). This ACM method is superior to previous methods in terms of simplicity, efficiency, and productivity of neural differentiation. The number of cells was increased 1000-fold, along with differentiation from ES cells into NSCs. NSCs can be highly purified without using either magnetic- or fluorescence-activated cell sorting, and incorporation of undifferentiated ES cells is virtually eliminated. Although low doses of undifferentiated mouse ES cells transplanted into rat striatum developed into fully differentiated DA neurons (Bjorklund et al., 2002), elimination of undifferentiated ES cells is crucial for reducing the risk of tumor formation. Consistent with our previous observations,

culture of NSCs derived from cynomolgus monkey ES cells on an adhesive substrate in ACM exclusively promoted differentiation into neurons.

Parkinsonian features were induced by intravenous administration of MPTP over a period of several months. MPTP causes slowly progressive loss of DA neurons in the substantia nigra, resulting in primates showing all the clinical signs of PD, including tremor, rigidity, akinesia, and postural instability (Wichmann and DeLong, 2003). We created bilateral striatal lesions but implanted cells unilaterally, so one side could serve as a control. Functional effects of the graft were evaluated by comparing PET images of the implanted putamen with those of the contralateral putamen. PET can be used to assess DA function in vivo (Brooks, 2004) by following increases in L-[β-^{11}C]DOPA uptake or [^{11}C]β-CFT binding, which are attributable to the expression of AADC and storage of DA in the putamen and thus indicate graft survival and development of DA neurons. In addition, functional DA release from the graft was demonstrated by imaging D_2 receptor occupancy. Degrees of decrease in striatal radioactivity of [^{11}C]raclopride after amphetamine challenge were significantly higher in the grafted putamen. Based on microdialysis studies, a 1% change in striatal [^{11}C]raclopride binding has been estimated to correspond to a $\geq$8% change in synaptic DA levels (Breier et al., 1997). We identified numerous TH neurons in the grafted putamen. Although small populations of TH neurons may be found in the primate striatum after creating lesions of the nigrostriatal dopaminergic pathways, most are located in the caudate and precommissural putamen (Mazloom and Smith, 2006). The dramatic increase in the number of TH-IR cells in the postcommissural putamen suggests that these TH-IR cells were derived from the graft and contributed to the restoration of dopaminergic function.

Behavioral recovery was modest at 12 weeks after implantation. More DA neurons and synaptic DA release might be necessary for apparent behavioral recovery. Improving neuronal survival and increasing axonal outgrowth would possibly improve the magnitude of the response to grafting. In this regard, the combination of cell replacement and neuroprotective strategies by gene delivery may be effective in preventing the loss of endogenous and grafted NSCs. Another possible explanation for incomplete behavioral recovery is that functional integration of DA neurons with the host circuitry may take place gradually. PD patients with implanted fetal DA neurons show continuous symptomatic improvements even after DA storage capacity in the striatum (measured by L-[β-^{11}C]DOPA PET) and response to DA-releasing agents has plateaued (Isacson et al., 2001; Piccini et al., 2000). With bilateral implantation, further amelioration of global parkinsonism (including enhanced spontaneous activity and improved balance) would be expected, since only 20% of thalamic projections from the basal ganglia are crossed in monkeys (Parent and Hazrati, 1995) and unilateral implantation would mainly affect contralateral limb movement. Monkeys did not display dyskinesia with or without L-dopa. This result supports previous observations that functional DA grafts do not independently generate abnormal DA responses (Bjorklund et al., 2002).

Given the recent successful isolation of nuclear-transferred ES cell lines (Tabar et al., 2008), our findings of efficient ES cell transplantation, expansion, and differentiation into functional DA neurons in the primate model have implications for ES cells as a donor source for cell therapy against PD.

ACKNOWLEDGMENTS

The authors thank Astellas Pharmaceuticals (Osaka, Japan) for providing FK506.

REFERENCES

Bjorklund LM, Sanchez-Pernaute R, Chung S, Andersson T, Chen IY, McNaught KS, Brownell AL, Jenkins BG, Wahlestedt C, Kim KS, Isacson O. 2002. Embryonic stem cells develop into functional dopaminergic neurons after transplantation in a Parkinson rat model. Proc Natl Acad Sci USA 99:2344–2349.

Breier A, Su TP, Saunders R, Carson RE, Kolachana BS, de Bartolomeis A, Weinberger DR, Weisenfeld N, Malhotra AK, Eckelman WC, Pickar D. 1997. Schizophrenia is associated with elevated amphetamine-induced synaptic dopamine concentrations: Evidence from a novel positron emission tomography method. Proc Natl Acad Sci USA 94:2569–2574.

Brooks DJ. 2004. Positron emission tomography imaging of transplant function. NeuroRx 1:482–491.

Chung S, Shin BS, Hwang M, Lardaro T, Kang UJ, Isacson O, Kim KS. 2006. Neural precursors derived from embryonic stem cells, but not those from fetal ventral mesencephalon, maintain the potential to differentiate into dopaminergic neurons after expansion in vitro. Stem Cells 24:1583–1593.

Hall VJ, Li JY, Brundin P. 2007. Restorative cell therapy for Parkinson's disease: A quest for the perfect cell. Semin Cell Dev Biol 18:859–869.

Huang SC, Barrio JR, Phelps ME. 1986. Neuroreceptor assay with positron emission tomography: Equilibrium versus dynamic approaches. J Cereb Blood Flow Metab 6:515–521.

Inoue N, Matsui H, Tsukui H, Hatanaka H. 1988. The appearance of a highly digitalis-sensitive isoform of Na+,K+-ATPase during maturation in vitro of primary cultured rat cerebral neurons. J Biochem (Tokyo) 104:349–354.

Isacson O, Bjorklund L, Pernaute RS. 2001. Parkinson's disease: Interpretations of transplantation study are erroneous. Nat Neurosci 4:553.

Jenner P. 2000. Factors influencing the onset and persistence of dyskinesia in MPTP-treated primates. Ann Neurol 47 (4 Suppl 1): S90–S99; discussion S99–S104.

Kim JH, Auerbach JM, Rodriguez-Gomez JA, Velasco I, Gavin D, Lumelsky N, Lee SH, Nguyen J, Sanchez-Pernaute R, Bankiewicz K, McKay R. 2002. Dopamine neurons derived from embryonic stem cells function in an animal model of Parkinson's disease. Nature 418:50–56.

Kish SJ, Shannak K, Hornykiewicz O. 1988. Uneven pattern of dopamine loss in the striatum of patients with idiopathic Parkinson's disease. Pathophysiologic and clinical implications. N Engl J Med 318:876–880.

Li JY, Christophersen NS, Hall V, Soulet D, Brundin P. 2008. Critical issues of clinical human embryonic stem cell therapy for brain repair. Trends Neurosci 31:146–153.

Liu SV. 2008. iPS cells: A more critical review. Stem Cells Dev 17:391–397.

Mazloom M, Smith Y. 2006. Synaptic microcircuitry of tyrosine hydroxylase-containing neurons and terminals in the striatum

of 1-methyl-4-phenyl-1,2,3,6-tetrahydropyridine-treated monkeys. J Comp Neurol 495:453–469.
Nakayama T, Momoki-Soga T, Inoue N. 2003. Astrocyte-derived factors instruct differentiation of embryonic stem cells into neurons. Neurosci Res 46:241–249.
Nakayama T, Momoki-Soga T, Yamaguchi K, Inoue N. 2004. Efficient production of neural stem cells and neurons from embryonic stem cells. Neuroreport 15:487–491.
Newman MB, Bakay RA. 2008. Therapeutic potentials of human embryonic stem cells in Parkinson's disease. Neurotherapeutics 5:237–251.
Parent A, Hazrati LN. 1995. Functional anatomy of the basal ganglia. I. The cortico-basal ganglia-thalamo-cortical loop. Brain Res Brain Res Rev 20:91–127.
Piccini P, Lindvall O, Bjorklund A, Brundin P, Hagell P, Ceravolo R, Oertel W, Quinn N, Samuel M, Rehncrona S, Widner H, Brooks DJ. 2000. Delayed recovery of movement-related cortical function in Parkinson's disease after striatal dopaminergic grafts. Ann Neurol 48:689–695.
Rodriguez-Gomez JA, Lu JQ, Velasco I, Rivera S, Zoghbi SS, Liow JS, Musachio JL, Chin FT, Toyama H, Seidel J, Green MV, Thanos PK, Ichise M, Pike VW, Innis RB, McKay RD. 2007. Persistent dopamine functions of neurons derived from embryonic stem cells in a rodent model of Parkinson disease. Stem Cells 25:918–928.
Sanchez-Pernaute R, Studer L, Ferrari D, Perrier A, Lee H, Vinuela A, Isacson O. 2005. Long-term survival of dopamine neurons derived from parthenogenetic primate embryonic stem cells (cyno-1) after transplantation. Stem Cells 23:914–922.
Suemori H, Tada T, Torii R, Hosoi Y, Kobayashi K, Imahie H, Kondo Y, Iritani A, Nakatsuji N. 2001. Establishment of embryonic stem cell lines from cynomolgus monkey blastocysts produced by IVF or ICSI. Dev Dyn 222:273–279.
Tabar V, Tomishima M, Panagiotakos G, Wakayama S, Menon J, Chan B, Mizutani E, Al-Shamy G, Ohta H, Wakayama T, Studer L. 2008. Therapeutic cloning in individual parkinsonian mice. Nat Med 14:379–381.
Takagi Y, Takahashi J, Saiki H, Morizane A, Hayashi T, Kishi Y, Fukuda H, Okamoto Y, Koyanagi M, Ideguchi M, Hayashi H, Imazato T, Kawasaki H, Suemori H, Omachi S, Iida H, Itoh N, Nakatsuji N, Sasai Y, Hashimoto N. 2005. Dopaminergic neurons generated from monkey embryonic stem cells function in a Parkinson primate model. J Clin Invest 115:102–109.
Tsukada H, Harada N, Nishiyama S, Ohba H, Kakiuchi T. 2000a. Cholinergic neuronal modulation alters dopamine D2 receptor availability in vivo by regulating receptor affinity induced by facilitated synaptic dopamine turnover: Positron emission tomography studies with microdialysis in the conscious monkey brain. J Neurosci 20:7067–7073.
Tsukada H, Harada N, Nishiyama S, Ohba H, Sato K, Fukumoto D, Kakiuchi T. 2000b. Ketamine decreased striatal [(11)C]raclopride binding with no alterations in static dopamine concentrations in the striatal extracellular fluid in the monkey brain: Multiparametric PET studies combined with microdialysis analysis. Synapse 37:95–103.
Watanabe M, Okada H, Shimizu K, Omura T, Yoshikawa E, Kosugi T, Mori S, Yamashita T. 1997. A high resolution animal PET scanner using compact PS-PMT detectors. IEEE Trans Nucl Sci 44:1277–1282.
Wichmann T, DeLong MR. 2003. Pathophysiology of Parkinson's disease: The MPTP primate model of the human disorder. Ann N Y Acad Sci 991:199–213.

Short Report

A convenient enzyme-linked immunosorbent assay for rapid screening of anti-adeno-associated virus neutralizing antibodies

Tetsuo Ito[1], Shigekazu Yamamoto[1], Tsukasa Hayashi[1], Mika Kodera[1,3], Hiroaki Mizukami[2], Keiya Ozawa[2] and Shin-ichi Muramatsu[3]

[1]KAINOS Laboratories Inc., Tokyo; [2]Division of Genetic Therapeutics; [3]Division of Neurology, Jichi Medical University, Tochigi, Japan
Corresponding author: Shin-ichi Muramatsu, 3311-1 Yakushiji, Shimotsuke, Tochigi 329-0498, Japan. Email: muramats@jichi.ac.jp

Abstract

Background: Recombinant adeno-associated virus vectors based on serotype 2 (AAV-2) have become leading vehicles for gene therapy. Most humans in the general population have anti-AAV-2 antibodies as a result of naturally acquired infections. Pre-existing immunity to AAV-2 might affect the functional and safety consequences of AAV-2 vector-mediated gene transfer in clinical applications.

Methods: An enzyme-linked immunosorbent assay (ELISA) method was developed using microwell plates coated with intact particles of recombinant AAV-2 vectors, and horseradish peroxidase-conjugated anti-human immunoglobulin G (HRP-IgG). Neutralizing antibody titres were analysed by assessing the ability of serum antibody to inhibit transduction into HEK293 cells of AAV vectors that express β-galactosidase.

Results: Anti-AAV-2 antibodies were detected by ELISA in two of 20 healthy subjects. The positivity criterion (optical density >0.5) in ELISA corresponded to the cut-off value (320-fold dilution of serum) in the AAV-2 neutralization assay. Influences of interfering substances were not observed.

Conclusion: This ELISA method may be useful for rapid screening of anti-AAV-2 neutralizing antibodies in candidates for gene therapy.

Ann Clin Biochem 2009; **46**: 508–510. DOI: 10.1258/acb.2009.009077

Introduction

Adeno-associated virus (AAV) is a small single-stranded DNA virus within the parvovirus family.[1,2] Among more than 100 genotypes of primate AAV, serotype 2 (AAV-2) is the most studied and was the first to be engineered for vector development. Recombinant AAV-2 vectors efficiently transduce both dividing and non-dividing cells and provide long-term gene expression without significant toxicity. Growing numbers of clinical trials have been conducted using AAV-2 vectors to combat various diseases. However, one major problem is the high prevalence of anti-AAV-2 antibodies in the human population. More than 90% of adults demonstrate antibodies that cross-react with one or more AAV serotypes, although markedly fewer (18–32%) show neutralizing antibodies (nAb).[3,4] Pre-existing immunity to AAV-2 may block transduction and intensify the innate response to vector administration, leading to a poor outcome of gene therapy. Thus, measurement of the anti-AAV-2 nAb titre is necessary.

Methods

Recombinant AAV-2 vectors were produced by the triple transduction method as described previously.[5] In brief, HEK293 cells were transfected with the following three plasmids: pAAV2-Rep/vp (containing the AAV-2 *rep* and *cap* genes), pAd (containing the adenovirus genome) and pW1 (containing the β-galactosidase-expression cassette). After three days of incubation, the transfected cells were frozen and thawed, and the recombinant AAV-2 vector particles that were released were purified by two sequential CsCl density gradient centrifugations.

Serum samples from healthy adults were purchased from Advanced BioServices LLC, (Reseda, CA, USA). AAV-specific antibodies were detected using an enzyme-linked immunosorbent assay (ELISA). Ninety-six-well microtitre plates (Invitrogen, Carlsbad, CA, USA) were coated with 0.5 μg (1.4×10^8 vector genomes [vg]) of AAV-2 vector particles per well. After blocking with 2% bovine serum albumin (BSA) in phosphate-buffered saline (PBS), the plates were washed with 2% sucrose. Serum samples diluted at 1:1000 with PBS/0.1% BSA were added to each well (100 μL/well). The plates were incubated for 1 h at room temperature (RT) and washed three times with PBS/0.05% Tween 20. A solution containing 1 μg/mL horseradish peroxidase-conjugated anti-human immunoglobulin G (HRP-IgG; self-prepared using a heterobifunctional

reagent) was added to each well (100 μL/well). The plates were incubated for 1 h at RT and washed three times with washing buffer. Colour was developed by adding 100 μL 3,3′,5,5′-tetramethylbenzidine/urea hydrogen peroxide (Neogen, Lexington, KY, USA) and incubating the plates for 30 min at RT. Colour development was stopped by adding 1 mol/L sulphuric acid (100 μL/well), and the optical density (OD) was measured at 450/640 nm. The optimum reaction conditions were determined in the following ranges: 0.5×10^8 to 3×10^8 vg of AAV-2 vector particles per well, 10- to 5000-fold dilution of the specimen and 0.01–0.4 μg/mL concentration of HRP-IgG. The effects of bilirubin, haemoglobin and chyle as endogenous interference materials were studied. Samples including these materials at 500 mg/L, 5000 mg/L and 3000°, respectively, were mixed with sera at a volume ratio of 1 : 9 and analysed by ELISA.

For the nAb assay, sera were continuously diluted two-fold with Dulbecco's Modified Eagle's Medium and Harn's F-12 Nutrient Mixture (DMEM/F12, Invitrogen) 10% fetal bovine serum (Sigma-Aldrich, St. Louis, MO, USA), 100 U/mL penicillin (Invitrogen) and 100 μg/mL streptomycin (Invitrogen). AAV-2 vectors were diluted with 10 mmol/L HEPES/130 mmol/L NaCl (pH 8.0) up to 1.4×10^8 vg/μL, and optimum transduction was obtained with 1.4×10^{10} vg/μL. Ten microlitres of diluted serum were added to 5 μL diluted AAV-2 vector, and the mixture was incubated for 1 h at RT. The mixture was then added to 96-well plates containing confluent HEK293 cells. Two days after transduction, β-galactosidase activity was measured with a β-galactosidase assay kit (Invitrogen). The titre of nAb was defined as the highest dilution of serum that showed <50% of the β-galactosidase activity of the negative control.

Results and discussion

In the ELISA method developed in this study, AAV-2 vector particles immobilized on plates captured AAV-2-specific antibodies. Using whole vector particles as antigens without degradation, antibodies that are more specific AAV-2, including nAb, can be assessed. Intra-assay precision was determined by repeatedly ($n = 8$) measuring four kinds of serum with different nAb titres. For three samples whose nAb titres were ×640, ×80 and ×80, the coefficient of variation (CV) of the OD was 2.5%, 4.3% and 1.8%, respectively. For the fourth sample, with ×10 titre, the average OD was 0.012 and the CV was 8.5%. These data confirm the good precision of the assay. The effects of interference materials were <10%, suggesting that the method had good specificity. All reagents, including AAV particles, were stable after storage for 13 months at 4°C, and sensitivity of the ELISA was maintained at 95% with fresh reagents.

The nAb titres for 20 healthy donor samples varied from ×10 to ×640, and 13 samples had a titre less than ×20. Using the ELISA method, the absorbance values of the samples varied from 0.012 to 0.752, and 15 samples showed absorbance of less than 0.08 (Table 1). In our study, a nAb titre higher than × 32 corresponded to an OD greater than 0.5 in the ELISA. If these values were used as cut-off points, two of 20 samples found to be positive in both the nAb assay and the ELISA. Further studies on more samples were necessary to validate the cut-off values in different populations.

Table 1 Correlation between a neutralizing antibody assay (nAb) and the ELISA method

	nAb assay		ELISA	
Sample ID	nAb titre	Decision	OD	Decision
1	10	Neg.	0.014	Neg.
2	80	Neg.	0.075	Neg.
3	10	Neg.	0.013	Neg.
4	10	Neg.	0.016	Neg.
5	160	Neg.	0.291	Neg.
6	80	Neg.	0.015	Neg.
7	80	Neg.	0.032	Neg.
8	10	Neg.	0.010	Neg.
9	10	Neg.	0.025	Neg.
10	10	Neg.	0.012	Neg.
11	10	Neg.	0.014	Neg.
12	80	Neg.	0.468	Neg.
13	10	Neg.	0.012	Neg.
14	320	Pos.	0.596	Pos.
15	640	Pos.	0.725	Pos.
16	10	Neg.	0.013	Neg.
17	20	Neg.	0.114	Neg.
18	10	Neg.	0.046	Neg.
19	10	Neg.	0.016	Neg.
20	10	Neg.	0.012	Neg.

OD, optical density; ELISA, enzyme-linked immunosorbent assay; nAb, neutralizing antibodies

AAV-2 antibody in 20 sera from healthy individuals was analysed by ELISA and a neutralizing antibody assay. The measured values were expressed as OD or titre. The cut-off value for the neutralizing antibody assay was provisionally fixed at ×320. The criterion for positivity for the ELISA method was considered greater than OD 0.5

Conclusion

We have developed a simple and convenient ELISA method for detecting serum anti-AAV-2 antibodies. Antibody titres assessed by this method show good correlation with nAb titres obtained in a cell transduction assay, suggesting that this ELISA may be useful for the rapid screening of nAbs in candidates for gene therapy.

DECLARATIONS

Competing interests: None.

Funding: Part of this work was supported by a grant (19591003) from the Ministry of Education, Science, Sports and Culture of the Japanese Government, and a grant (20261501) from the Japan Ministry of Health, Labour and Welfare.

Ethical approval: The ethics committee of Jichi Medical University approved this study (GT-001).

Guarantor: SM.

Contributorship: Conceived and designed the experiments: SM, HM, TI, TH. Performed the experiments: TY, MK, HM, Analysed the data: TI, SY, TH, MK, HM, KO, SM, Wrote the paper: TI, SM.

REFERENCES

1 Gao G, Vandenberghe LH, Alvira MR, *et al.* Clades of adeno-associated viruses are widely disseminated in human tissues. *J Virol* 2004;**78**:6381–8
2 Wu Z, Asokan A, Samulski RJ. Adeno-associated virus serotypes: vector toolkit for human gene therapy. *Mol Ther* 2006;**14**:316–27
3 Chirmule N, Propert K, Magosin S, *et al.* Immune responses to adenovirus and adeno-associated virus in humans. *Gene Ther* 1999;**6**:1574–83
4 Moskalenko M, Chen L, van Roey M, *et al.* Epitope mapping of human anti-adeno-associated virus type 2 neutralizing antibodies: implications for gene therapy and virus structure. *J Virol* 2000;**74**:1761–6
5 Li XG, Okada T, Kodera M, *et al.* Viral-mediated temporally controlled dopamine production in a rat model of Parkinson disease. *Mol Ther* 2006;**13**:160–6

(Accepted 24 June 2009)

OPEN ACCESS Freely available online

PLoS one

Ablation of NMDA Receptors Enhances the Excitability of Hippocampal CA3 Neurons

Fumiaki Fukushima[1], Kazuhito Nakao[1], Toru Shinoe[2¤a], Masahiro Fukaya[3], Shin-ichi Muramatsu[4], Kenji Sakimura[5], Hirotaka Kataoka[1], Hisashi Mori[1¤b], Masahiko Watanabe[3], Toshiya Manabe[2,6], Masayoshi Mishina[1]*

1 Department of Molecular Neurobiology and Pharmacology, Graduate School of Medicine, University of Tokyo, Tokyo, Japan, **2** Division of Neuronal Network, Institute of Medical Science, University of Tokyo, Tokyo, Japan, **3** Department of Anatomy, Hokkaido University School of Medicine, Sapporo, Japan, **4** Division of Neurology, Department of Medicine, Jichi Medical University, Tochigi, Japan, **5** Department of Cellular Neurobiology, Brain Research Institute, Niigata University, Niigata, Japan, **6** CREST, JST, Kawaguchi, Japan

Abstract

Synchronized discharges in the hippocampal CA3 recurrent network are supposed to underlie network oscillations, memory formation and seizure generation. In the hippocampal CA3 network, NMDA receptors are abundant at the recurrent synapses but scarce at the mossy fiber synapses. We generated mutant mice in which NMDA receptors were abolished in hippocampal CA3 pyramidal neurons by postnatal day 14. The histological and cytological organizations of the hippocampal CA3 region were indistinguishable between control and mutant mice. We found that mutant mice lacking NMDA receptors selectively in CA3 pyramidal neurons became more susceptible to kainate-induced seizures. Consistently, mutant mice showed characteristic large EEG spikes associated with multiple unit activities (MUA), suggesting enhanced synchronous firing of CA3 neurons. The electrophysiological balance between fast excitatory and inhibitory synaptic transmission was comparable between control and mutant pyramidal neurons in the hippocampal CA3 region, while the NMDA receptor-slow AHP coupling was diminished in the mutant neurons. In the adult brain, inducible ablation of NMDA receptors in the hippocampal CA3 region by the viral expression vector for Cre recombinase also induced similar large EEG spikes. Furthermore, pharmacological blockade of CA3 NMDA receptors enhanced the susceptibility to kainate-induced seizures. These results raise an intriguing possibility that hippocampal CA3 NMDA receptors may suppress the excitability of the recurrent network as a whole *in vivo* by restricting synchronous firing of CA3 neurons.

Citation: Fukushima F, Nakao K, Shinoe T, Fukaya M, Muramatsu S-i, et al. (2009) Ablation of NMDA Receptors Enhances the Excitability of Hippocampal CA3 Neurons. PLoS ONE 4(1): e3993. doi:10.1371/journal.pone.0003993

Editor: Frederic Andre Meunier, The University of Queensland, Australia

Received September 4, 2008; **Accepted** December 3, 2008; **Published** January 14, 2009

Funding: This work was supported in part by Grant-in-Aid for Scientific Research on Priority Areas (Molecular Brain Science) and Global COE Program (Integrative Life Science Based on the Study of Biosignaling Mechanisms) from the Ministry of Education, Culture, Sports, Science and Technology of Japan. F.F. was supported by Japan Society for the Promotion of Science, and S.T. by the 21st Century COE Program, the Ministry of Education, Culture, Sports, Science and Technology of Japan. The funders had no role in study design, data collection and analysis, decision to publish, or preparation of the manuscript.

Competing Interests: The authors have declared that no competing interests exist.

* E-mail: mishina@m.u-tokyo.ac.jp

¤a Current address: Division of Molecular and Developmental Biology, Institute of Medical Science, University of Tokyo, Tokyo, Japan,
¤b Current address: Department of Molecular Neuroscience and Pharmaceutical Sciences, Graduate School of Medicine, University of Toyama, Toyama, Japan

Introduction

Hippocampal CA3 pyramidal neurons form abundant recurrent connections with other CA3 neurons [1,2]. The activity of single pyramidal neurons spreads to other CA3 neurons and this facilitates the rapid synchronization of action-potential firing in CA3 neurons [3]. Synchronized discharges of hippocampal CA3 neurons are supposed to underlie network oscillations [4], memory consolidation [5] and seizure generation [6]. Physiological sharp wave (SPW) activity that occurs during slow-wave sleep and behavioral immobility is dependent on synchronous discharges by population of CA3 pyramidal neurons [7,8]. Synchronized CA3 activity may also contribute to the pathological EEG pattern, known as an interictal spike, which indicates a propensity for temporal lobe seizures [6].

NMDA receptors play key roles in synaptic plasticity and memory [9]. In the CA3 network, NMDA receptors are abundant at the commissural/associational synapses but scarce at the mossy fiber synapses [10]. Thus, the CA3 recurrent network is under the control of NMDA receptors. NMDA receptors in the hippocampal CA3 region are implied in rapid acquisition and recall of associative memory as well as paired associate learning [11–13]. On the other hand, studies with hippocampal slices showed that the synchronous network activity induces NMDA receptor-dependent LTP of CA3 recurrent synapses [14] and that stimuli that induced NMDA receptor-dependent LTP in the CA3 region generated sharp wave-like synchronous network activity [15]. These *in vitro* observations raised the hypothesis that the NMDA receptor-mediated LTP contributes to the generation of synchronous network activity. Here, we generated hippocampal CA3 pyramidal neuron-specific NMDA receptor mutant mice on the pure C57BL/6N genetic background. The ablation of hippocampal CA3 NMDA receptors resulted in the enhancement of the susceptibility to kainate-induced seizure and the emergence of characteristic large EEG spikes. We also showed that the virus-mediated ablation of hippocampal CA3 NMDA receptors in the

adult mice generated characteristic large EEG spikes and that pharmacological blockade of CA3 NMDA receptors enhanced the susceptibility to kainate-induced seizures. These results raise an intriguing possibility that NMDA receptors may control negatively the excitability of the hippocampal CA3 recurrent network as a whole *in vivo*.

Methods

Generation of mice

Genomic DNA carrying the exon 11 to 22 of the *GluRζ1* gene was isolated by screening a bacterial artificial chromosome (BAC) library prepared from the C57BL/6 strain (Incyte Genomics) with the 2.2 kb-*Eco*RI fragment from pBKSAζ1 [16]. The 13.3-kb *Eco*RI-*Xba*I fragment of the BAC clone was used for construction of the targeting vector. The *loxP* site was inserted into the *Bam*HI site between exon 18 and 19, and the 1.8-kb DNA fragment carrying the *loxP* sequence and *Pgk-1* promoter-driven neomycin phosphotransferase gene (*neo*) flanked by two Flp recognition target (*frt*) sites into the *Spe*I site between exon 20 and 21. Endogenous *Eco*RI site at the 5′ end of 13.3-kb *Eco*RI-*Xba*I genomic fragment was replaced with *Not*I site and an exogenous *Eco*RI site was inserted between the second *loxP* site and *neo* gene. The targeting vector pζ1TV was composed of the 14.8-kb *Not*I-*Xba*I fragment, MC1 promoter-driven diphteria toxin gene derived from pMC1DTpA and pBluescript II SK(+) [17]. The targeting vector was linearized by *Not*I and electroporated into ES cells derived from the C57BL/6N strain [18,19]. Recombinant clones were identified by Southern blot analysis of *Eco*RI-digested genomic DNA using 284-bp fragment amplified with primers 5′-ATAGA-GAAAGACATGGGGC-3′ and 5′-TGCTACTGTGCAG-GAAGTG-3′ from pζ1TV, the 0.6 kb *Pst*I fragment from pLFNeo [20], and the 1.1-kb *Xho*I–*Eco*RI fragment from the BAC clone as 5′ inner, neo, and 3′ outer probes, respectively. The $GluR\zeta1^{flox}$ allele was also identified by PCR using primers 5′-GCAGT-GAGGCTCACACAGGCCTGAAGACTA-3′ and 5′-AGT-GAACTCGGATCCTGACCATTGGCCACT-3′. Chimeric mice production and elimination of the *neo* gene from the genome through Flp/frt-mediated excision were carried out essentially as described [18–20].

GluRγ1-Cre mice were obtained by inserting the *cre* gene in the translational initiation site of the *GluRγ1* gene in frame using ES cells derived from the C57BL/6N strain [19]. The 1.8-kb DNA fragment, which carried the polyadenylation signal sequence and *pgk-1* promoter-driven *neo* gene flanked by two *frt* sites [20], was inserted into the downstream of the *cre* gene. $GluR\zeta1^{+/flox}$ mice were crossed with GluRγ1-Cre mice to yield $GluR\gamma1^{+/cre}$; $GluR\zeta1^{flox/flox}$ mice. The $GluR\gamma1^{+/cre}$ allele was identified by PCR using primers 5′-AACTGCAGTCTTGCATGCTCTCTG-GAGCC-3′, 5′-GGAGCGGAGACACGGGGCAT-3′ and 5′-TTGCCCCTGTTTCACTATCC-3′. Cre recombinase-mediated NMDA receptor ablation is hippocampal CA3 pyramidal neuron-specific in $GluR\gamma1^{+/cre}$; $GluR\zeta1^{flox/flox}$ mice (Fig. 1). It is unknown why the *GluRγ1* promoter-driven Cre expression does not exactly follow the expression pattern of GluRγ1 [21]. The insertion of the *pgk-1* promoter-driven *neo* gene and the polyadenylation signal sequence together may affect the Cre expression pattern since the elimination of the *neo* gene through Flp-mediated recombination altered the expression pattern.

All animal procedures were approved by the Animal Care and the Use Committee of Graduate School of Medicine, the University of Tokyo (Approval # 1721T062). Mice were fed *ad libitum* with standard laboratory chow and water in standard animal cages under a 12 h light/dark cycle.

AAV-Cre vector

We employed AAV to deliver Cre recombinase since AAV is safe, non-pathogenic, non-inflammatory and extremely stable stable [22,23]. AAV-Cre or AAV-EGFP vector contains an expression cassette consisting of a human cytomegalovirus immediate-early promoter (CMV promoter), followed by the human growth hormone first intron, cDNA of Cre recombinase with a nuclear localization signal or the enhanced green fluorescence protein (EGFP), and simian virus 40 polyadenylation signal sequence (SV40 polyA), between the inverted terminal repeats (ITR) of the AAV-2 genome. The two helper plasmids, pAAV-RC and pHelper (Agilent Technologies, Santa Clara, California), harbor the AAV *rep* and *cap* genes, and the *E2A*, *E4*, and *VA RNA* genes of the adenovirus genome, respectively. HEK293 cells were cotransfected by the calcium phosphate coprecipitation method with the vector plasmid, pAAV-RC, and pHelper. AAV vectors were then harvested and purified by two sequential continuous iodoxale ultracentrifugations. The vector titer was determined by quantitative DNA dot-blot hybridization or quantitative PCR of DNase-I-treated vector stocks. Before administration, AAV vectors were diluted in phosphate-buffered saline to $5–8\times10^{10}$ genome copies/μl. A glass micropipette was inserted into the hippocampal CA3 region of ketamine-anesthetized mice (AP, L, V = −1.2, ±1.2, +2.0; −1.7, ±2.0, +2.1; −2.2, ±2.5, +2.4; −2.7, ±3.2, +3.5; −3.2, ±2.5, +4.0). Two minutes after the insertion, 1.0 μl of a virus solution or vehicle was injected at a constant flow rate of 16.6 nl/min, and the glass micropipette was left in this configuration for an additional 2 min, to prevent reflux of the injected material along the injection track, before being slowly retracted. AAV spread 0.5–0.7 mm both rostrodorsally and laterally. For every injected animal, the limit of the infected region was verified by immunohistochemistry for Cre recombinase or GluRζ1.

Immunological analysis

Immunohistochemistry was done as described [24] using antibodies against VGluT2 (guinea pig) [25], Calbindin (rabbit) [26], PSD-95 (rabbit) [27], GluRα1 (rabbit) [28], GAD (guinea pig) [29], and Cre recombinase (1:1000; rabbit; Novagen). Immunobloting analyses in whole-brain homogenate were carried out using antibodies for GluRζ1 (rabbit) [30], and neuron-specific enolase (1:4000; Chemicon) and chemiluminescense (Amersham Biosciences).

Golgi staining

Coronal brain sections (2 mm) were immersed for 4 days in a solution composed of 5% glutaraldehyde (Wako) and 2% $K_2Cr_2O_7$ (Sigma) and then transferred to a 0.75% solution of $AgNO_3$ (Sigma) for further 4 days. The treated brain was sectioned (100 μm), dehydrated and mounted on glass slides.

Morphology of AAV-EGFP infected CA3 neurons

AAV-EGFP vector was delivered into the hippocampal CA3 region of ketamine-anesthetized control and mutant mice of 8 weeks old. Fourteen days later, fixed coronal brain sections (150 μm) were prepared. Neurons were examined with a Leica SP-5 confocal laser scanning microscope. Optical sections were collected at intervals of 0.15 μm and averaged 16 times using a 100×objective (N.A. 1.4). The distance between axonal varicosities was measured from 50 μm-portions of CA3 axons within the CA3 stratum radiatum [31]. For spine analysis, only spines on clearly visible tertiary apical and basal branches were imaged. During the quantitation of the spine density, putative spines in the

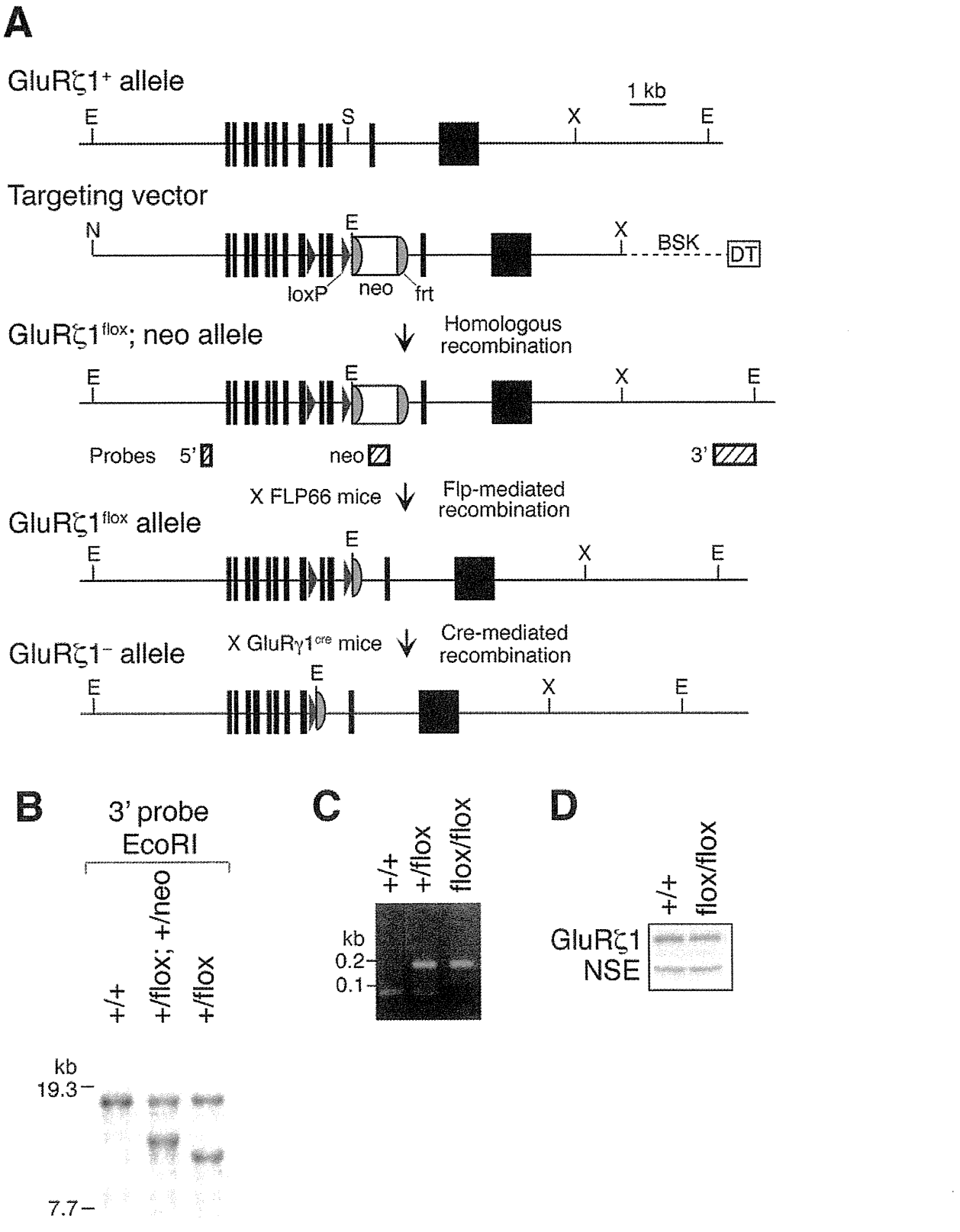
A
GluRζ1+ allele
1 kb
E
S
X
E
Targeting vector
N
E
X
BSK
DT
loxP
neo
frt
GluRζ1flox; neo allele
Homologous recombination
E
E
X
E
Probes 5'
neo
3'
X FLP66 mice
Flp-mediated recombination
GluRζ1flox allele
E
E
X
E
GluRζ1− allele
X GluRγ1cre mice
Cre-mediated recombination
E
E
X
E
B
3' probe
EcoRI
+/+
+/flox; +/neo
+/flox
kb
19.3
7.7
C
+/+
+/flox
flox/flox
kb
0.2
0.1
D
+/+
flox/flox
GluRζ1
NSE

Figure 1. Generation of *GluRζ1*^{flox} mice by homologous recombination in C57BL/6 strain derived ES cells. A, Schema of the exons 11–22 region of the *GluRζ1* gene (*GluRζ1*$^{+}$), targeting vector, floxed and *neo*-inserted allele (*GluRζ1*^{flox}; *neo*), and floxed allele (*GluRζ1*^{flox}). Exons 19 and 20 encode the putative transmembrane segment M4 of GluRζ1. The *GluRζ1*^{flox}; *neo* allele contains two *loxP* sequences flanking exons 19 and 20 of the *GluRζ1* gene and the *neo* gene flanked by two *frt* sequences. The *neo* gene was removed *in vivo* by crossing *GluRζ1*$^{+/flox}$; +/*neo* mice with FLP66 mice carrying the Flp recombinase gene under the control of the *EF1α* promoter. *GluRζ1*$^{+/flox}$ mice were crossed with GluRγ1-Cre mice to disrupt the GluRζ1 gene selectively in the hippocampal CA3 region. Abbreviations: BSK, plasmid pBluescript; DT, diphtheria toxin gene; neo, neomycin phosphotransferase gene; E, *Eco*RI; N, *Not*I; S, *Spe*I; X, *Xba*I. Hatched boxes indicate the location of probes for Southern blot analysis. **B**, Southern blot analysis of genomic DNA from *GluRζ1*$^{+/+}$, *GluRζ1*$^{+/flox}$; +/*neo*, and *GluRζ1*$^{+/flox}$ mice. *Eco*RI-digested DNA was hybridized with 3′ probe. **C**, Agarose gel electrophoresis of DNA fragments amplified by PCR from *GluRζ1*$^{+/+}$, *GluRζ1*$^{+/flox}$ and *GluRζ1*$^{flox/flox}$ mice. The amplified DNA fragments derived from the *GluRζ1*$^{+}$ and *GluRζ1*^{flox} alleles were 61 bp and 169 bp, respectively. **D**, Western blot analysis of GluRζ1 and neuron-specific enolase (NSE) proteins in whole-brain homogenates from *GluRζ1*$^{+/+}$ and *GluRζ1*$^{flox/flox}$ mice.
doi:10.1371/journal.pone.0003993.g001

three-dimensional reconstructed image were compared with both the unprocessed, individual optical sections and with a 'movie', in which segments of the three-dimensional reconstruction were rotated around the dendritic axis (IMARIS, Bitplane). For dendritic analysis, neurons were imaged on a Leica SP-5 with a 40×objective (N.A. 0.8). Optical sections were collected at intervals of 2 μm and averaged 8 times. The topographical order of the dendritic tree was made using the semi-automated program FilamentTracer (Bitplane). Analysis of dendritic topology included dendritic branches up to the third order. Analysis of dendritic spines was performed in rather linear, apical secondary and tertiary dendrites.

In situ hybridization

Isotopic detection of mRNAs was performed as described [32]. All samples were subjected to hybridization analysis at the same time and sections were exposed to a single x-ray film for measurement of relative optical density with IP Lab software. The relative expression levels of the mRNAs in the hippocampal CA3 region were calculated using the ratio of the density in the CA3 region to that of the CA1 region, except that the *GluRγ1* mRNA density in the CA3 region was directly compared between control and mutant mice. Double *in situ* hybridization was performed with mixture of [^{33}P]dATP-labeled oligonucleotide probe for GluRζ1 (complementary to residues 2583–2627, GenBank accession No. D10028) and digoxigenin (DIG)-labeled cRNA probe for GAD67 (complementary to residues 802–1617, No. A28072) as described [33]. Hybridization signals were visualized with nuclear track emulsion (NTB-2, Kodak) and fluorescent substrate (HNPP Fluorescent Detection Set, Boehringer-Mannheim), respectively. Sections were counterstained with NeuroTrace 500/525 green (Molecular Probes).

Kainate-induced seizure

Kainate was intraperitoneally administered to mice, and they were monitored for 1 h to determine whether they exhibited seizures with generalized tonic-clonic activity accompanying the loss of postural tone. Mice were then fixed under deep pentobarbital anesthesia for immunohistochemical analysis with the c-Fos antibody (Oncogene) 2 h after kainate administration.

Electrophysiology

Transverse hippocampal slices (400 μm thick) were superfused with an artificial cerebrospinal fluid (aCSF) containing (in mM): 119 NaCl, 2.5 KCl, 2.5 $CaCl_2$, 1.3 $MgSO_4$, 1 NaH_2PO_4, 26.2 $NaHCO_3$, and 11 glucose, which was equilibrated with 95% O_2/5% CO_2. Synaptic responses were evoked via a bipolar stimulating electrode placed in the CA3 stratum radiatum and whole-cell recordings were made from CA3 pyramidal cells using the blind-patch technique. The stimulus strength was set at the beginning of each experiment so that the average amplitude of synaptic responses in the absence of any antagonists is around 200 pA at a holding potential of −80 mV. The AMPA receptor-mediated excitatory postsynaptic current (AMPA-EPSC) was isolated by subtracting the synaptic response in the presence of 10 μM 6-cyano-7-nitroquinoxaline-2,3-dione (CNQX) from that in its absence. The NMDA receptor-mediated excitatory postsynaptic current (NMDA-EPSC) was recorded at +50 mV in the presence of 10 μM CNQX and 0.1 mM picrotoxin. The $GABA_A$ receptor-mediated inhibitory postsynaptic current ($GABA_A$-IPSC) was recorded at 0 mV in the presence of 10 μM CNQX and 25 μM D-2-amino-5-phosphonovaleric acid (D-APV). The stimulus strength was constant throughout each experiment. The slow hyperpolarizing currents induced by high-frequency stimulation (50 Hz, 40 pulses) were recorded at −20 mV in the presence of 0.1 mM picrotoxin as described previously [34]. Patch electrodes were filled with an internal solution containing (in mM): 140 potassium methansulfonate, 8 NaCl, 10 HEPES, 2 MgATP, and 0.3 Na_3-GTP (pH 7.2 adjusted with KOH, osmolarity 290 to 300 mOsm). For pharmacological experiments, 10 mM BAPTA was added in the pipette solution or potassium methansulfonate in the pipette solution was replaced by cesium methansulfonate. Voltage-clamped responses were recorded with an Axopatch 1D amplifier (Axon Instruments, Union City, CA, USA) and the signal was filtered at 1 kHz, digitized at 2.5 kHz, and stored on a personal computer.

Field potential recording *in vivo*

Urethane-anesthetized mice (1 g/kg body weight, i.p.) were fixed in a stereotaxic head holder (Narishige). For the recording of local field potentials, a tungsten electrode (2–5 MΩ, Frederick Haer) or a silicon probe (16 recoding sites with 50 μm separation, NeuroNexus Technologies) was inserted into the hippocampal CA3 region (AP = −2.0 mm from bregma, L = ±2.3 mm from midline, and V = +2.0 mm ventral to dura), the hippocampal CA1 region (AP = −2.0, L = ±1.0, V = +1.2) or the dentate gyrus (AP = −2.0, L = ±1.0, V = +2.0). Signals were amplified (MEG-1200, Nihon Kohden), band-pass filtered (0.08–1,000 Hz), digitized at 1 kHz through an AD converter (National Instruments), and stored in a computer. Analyses of data were performed offline using LabVIEW (National Instruments) and IGOR (Wave matics) software. Recordings using a glass electrode (10–15 MΩ, GD-2, Narishige) were carried out as described [35]. Raw traces (0.08–3,000 Hz) were band-pass filtered for the detection of MUA of neurons (0.15–3 kHz). EEG spikes with power of twice the s.d. from the baseline mean and the duration of about 30 ms were extracted. The unit activity was defined as a power of more than five times the s.d. from the baseline mean and the duration of less than 4 ms [7]. The locations of the electrode were verified histologically. CSD analyses were carried out as described [8].

Pharmacological experiments. Mice were anesthetized with ketamine (80 mg/kg, i.p.; Sankyo Co., Tokyo, Japan) and xylazine (20 mg/kg i.p.; Bayer, Tokyo, Japan), and fixed to a

stereotaxic apparatus (David Kopf, Tujunga, CA, USA). Two single guide cannulae (Plastics One, Roanoke, VA, USA) were implanted into the CA3 region of the hippocampus bilaterally (stereotaxic coordinates: AP = −2.2 mm from bregma, ML = ±2.5 mm from midline, DV = +1.4 mm from bregma), according to an atlas of the mouse brain [36]. The tip of the internal cannula for microinjection was inserted 1 mm below the tip of the guide cannulae (DV = +2.4 mm from bregma). The cannulae were fixed to the skull with dental cement. The animals were allowed to recover for at least 5 days. D,L-APV (Sigma-Aldrich, MO, USA) was dissolved in aCSF at a concentration of 30 mM. The aCSF was consisted of NaCl (150 mM), KCl (3 mM), $CaCl_2$ (1.4 mM), $MgCl_2$ (0.8 mM), Na_2HPO_4 (0.8 mM), and NaH_2PO_4 (0.2 mM). During drug infusions, the mice were restrained lightly in the disposable vinyl jacket (Braintree Scientific, Inc, MA, USA) and 0.5 µl of the drug or aCSF was infused at a rate of 0.2 µl/min using a microinjection pump (CMA/100, CMA/Microdialysis, Solna, Sweden). The infusion cannulae (bilateral) were left in place for a further 1 min to diffuse the drug from the needle tip, and the animal was then returned to its home cage. Kainate was delivered i.p. 20–30 min after APV injection.

Statistical analysis

All behavioral experiments were performed in a blind fashion. Data were expressed as mean±SEM. Statistical analysis was performed using Fisher's exact probability test, Kolmogorov-Smirnov test, log-rank test and Student *t*-test as appropriate. Statistical significance was set at $p<0.05$.

Results

Selective ablation of NMDA receptors in hippocampal CA3 pyramidal neurons

We disrupted the NMDA receptor *GluRζ1/NR1* gene specifically in the hippocampal CA3 pyramidal cells by Cre-*loxP* recombination on the C57BL/6N genetic background. By crossing a target mouse line carrying two *loxP* sequences flanking exon 19 and 20 of the *GluRζ1* gene (*GluRζ1*$^{+/flox}$ mice) with a hippocampal CA3 region-dominant Cre mouse line carrying the Cre recombinase gene inserted into the *GluRγ1/KA-1* gene (GluRγ1-Cre mice), we obtained *GluRγ1*$^{+/cre}$; *GluRζ1*$^{flox/flox}$ mice and *GluRζ1*$^{flox/flox}$ mice (Fig. 1), and used them in subsequent experiments as mutant and control mice, respectively.

In situ hybridization signals for the *GluRζ1* mRNA were indistinguishable between mutant and control mice at postnatal day 1 (P1) (Fig. 2A). At P7, *GluRζ1* signals were diminished specifically in the hippocampal CA3 region of mutant mice (Fig. 2B). At P21 to P23, the hybridization signals were hardly detectable in the CA3 region of mutant mice and slightly decreased in the brainstem (Fig. 2C). Residual hybridization signals for the *GluRζ1* mRNA were co-localized with those of the *GAD67* mRNA, suggesting that expression of the *GluRζ1* mRNA was intact in CA3 interneurons (Fig. 2G, $n = 17$ out of 17 GAD67-positive cells). Immunohistochemical analyses showed that immunoreactivity for GluRζ1 protein was present in the CA3 region at P7, though the amount appeared to be decreased (Fig. 2D). However, the expression of GluRζ1 protein was diminished to a negligible level at P14 and P21 (Fig. 2E and F).

We examined NMDA-EPSCs by whole-cell patch-clamp recordings from the pyramidal cell in the CA3 region of the hippocampus at P21 to P23. NMDA-EPSCs were evoked by stimulating associational/commissural fibers that mainly terminate in the stratum radiatum since NMDA receptors are more

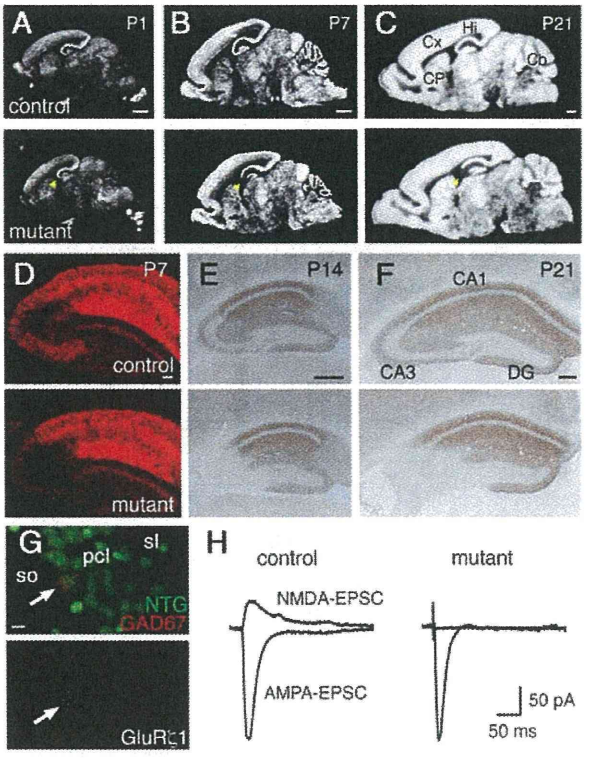

Figure 2. Generation of CA3 pyramidal neuron-selective NMDA receptor knockout mice. A–C, X-ray film autoradiography for *GluRζ1* mRNAs. Arrowheads indicate the CA3 region. **D–F**, Immunohistochemistry for GluRζ1 proteins. **G**, Double *in situ* hybridization for *GluRζ1* (white) and *GAD67* mRNA (red), counterstained with neurotrace green (green), in the mutant CA3 region. Arrow indicates a neuron expressing both *GluRζ1* and *GAD67* mRNAs. Scale bars: **A–C**, 1 mm; **D–F**, 200 µm; **G**, 10 µm. Abbreviations: Cb, cerebellum; CP, caudate-putamen; Cx, cortex; DG, dentate gyrus; Hi, hippocampus; pcl, pyramidal cell layer; sl, stratum lucidum; so, stratum oriens. **H**, Representative traces of AMPA- and NMDA-EPSCs at CA3 commissural/associational synapses.
doi:10.1371/journal.pone.0003993.g002

abundantly expressed in the stratum radiatum than in the stratum lucidum (Fig. 2H). In mutant mice, NMDA-EPSCs were not detectable, while AMPA-EPSCs were normally evoked. The ratios of the amplitudes of NMDA-EPSCs to those of AMPA-EPSCs were 50.9±16.1% (mean±s.e.m.) in control mice and 0.2±0.2% in mutant mice ($n = 4$ each; *t*-test, $P = 0.03$). Thus, NMDA receptors were abolished in hippocampal CA3 pyramidal neurons of mutant mice by P21. We used mutant and control mice at P21 to P23 in the following experiments unless otherwise specified.

Enhanced susceptibility of mutant mice to kainate-induced seizure

To monitor the excitability of CA3 recurrent circuits *in vivo*, we tested the kainate sensitivity of mutant mice since the administration of kainate to rodents stimulates initially the CA3 region and then generates seizures [37]. Intraperitoneal administration of kainate at 8 mg/kg induced tonic-clonic seizures with loss of the postural tone in mutant mice within 1 h, but not in control mice (Fig. 3A, $P<0.001$, Fisher's exact probability test). Mice of both genotypes showed seizures at a higher dosage of kainate (12 mg/kg), but the latency to the onset of seizures was significantly shorter in mutant mice (Fig. 3B, $P = 0.03$, log-rank test). Neither mutant

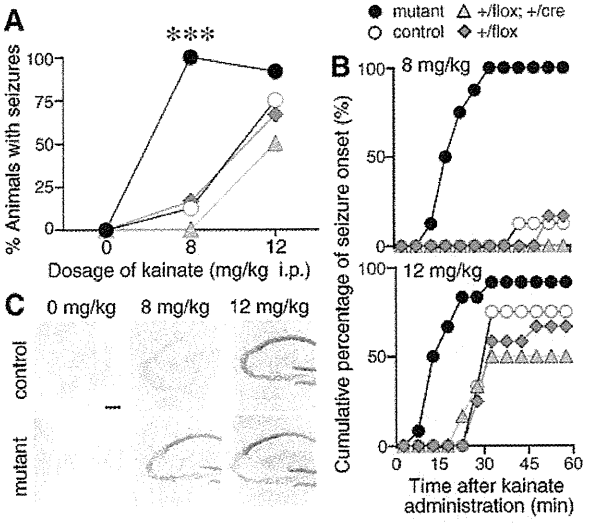

Figure 3. Increased susceptibility to kainate-induced tonic-clonic seizures in the mutant mice. A, The graph represents the percentage of mice with the generalized tonic-clonic seizures 1 h after drug administration. ***, $P<0.001$, Fisher's exact probability test. **B**, Cumulative curves for the onset of seizure. Saline, $n=4$–6; 8 mg/kg, $n=7$–8; 12 mg/kg, $n=12$. **C**, c-Fos immunohistochemistry in the hippocampus. Scale bar, 200 μm.
doi:10.1371/journal.pone.0003993.g003

nor control mice showed seizures after saline-administration. These results suggest that kainate-induced seizure susceptibility was enhanced in mutant mice. Susceptibility to the seizure was comparable between control *GluRζ1*$^{flox/flox}$ mice and *GluRγ1*$^{+/cre}$; *GluRζ1*$^{+/flox}$ mice, indicating that the insertion of the *Cre* gene in one allele of *GluRγ1* locus did not influence the susceptibility.

To monitor the neuronal activity *in vivo*, we employed c-Fos immunohistochemistry. There was little c-Fos immunoreactivity in the hippocampus of both control and mutant mice administrated with saline ($n=3$, Fig. 3C). Administration of kainate at 8 mg/kg induced strong c-Fos-immunoreactivity in the hippocampus of mutant mice ($n=3$). In contrast, no significant immunoreactivity was detectable in the hippocampus of kainate-administrated control mice ($n=3$). Kainate at 12 mg/kg induced strong c-Fos immunoreactivity in both control and mutant mice with seizures, while the number of Fos-immunopositive cells in the hippocampus was significantly smaller in mutant mice than in control mice ($n=20$ sections from 5 mice). The cellular imaging of neural activity with c-Fos immunohistochemistry confirmed the enhanced seizure susceptibility of mutant mice.

Histological features of the hippocampal CA3 region

Unexpectedly, we found that mutant mice lacking NMDA receptors selectively in CA3 pyramidal neurons became more susceptible to kainate-induced seizures. One obvious possibility is that the ablation of NMDA receptors may disturb the neural wiring of the hippocampal CA3 region, leading to abnormal excitability of the network. We thus examined the histological features of the hippocampal CA3 region in detail. The laminar organization and cellular distribution of the hippocampal CA3 region examined by Nissl staining was indistinguishable between control and mutant mice (Fig. 4A). Immunostaining for vesicular glutamate transporter 2 (VGluT2) and calbindin showed that the afferent terminals from the entorhinal cortex and the dentate gyrus were localized in the stratum lacunosum-moleculare and the stratum lucidum in both control and mutant mice, respectively (Fig. 4B and C).

Golgi staining revealed no appreciable differences in dendritic arborization of CA3 pyramidal cells between control and mutant mice (Fig. 4G). There were no significant differences in the numbers of branch points (control, 16.6±1.1, $n=8$; mutant, 17.0±1.1, $n=9$; $P=0.80$; *t*-test) and the primary (control, 4.4±0.5; mutant, 3.8±0.6; $P=0.45$), secondary (control, 7.8±0.7; mutant, 7.0±0.7; $P=0.49$) and tertiary dendrites (control, 9.4±1.4; mutant, 9.9±1.0; $P=0.76$) between two genotypes (Fig. 4I and J). Mean spine density on basal dendrites of CA3 pyramidal cells was also comparable ($n=28$ dendrites from 3–4 mice, $P=0.15$) (Fig. 4H and K). Consistent with Golgi staining, fine structures of CA3 neurons visualized by EGFP expression revealed no detectable alteration in terms of dendritic arborization and the distribution of presynaptic axonal boutons and postsynaptic spines (Fig. 5).

Immunoreactivities for postsynaptic proteins, PSD-95 and GluRα1/GluR1, were comparable in the hippocampal CA3 region between the two genotypes (Fig. 4D and E). Distribution of interneurons in the hippocampal CA3 and hilar areas was also indistinguishable as judged by immunostaining for GAD proteins (Fig. 4F), parvalbumin, somatostatin and calretinin. Thus, the histological and cytological organizations of the hippocampal CA3 region were indistinguishable between control and mutant mice.

Characteristic EEG spikes associated with multiple unit activities in the hippocampal CA3 region of mutant mice

Since seizure is produced by synchronous firing of a population of neurons in the brain [38], it is possible that NMDA receptor ablation in the CA3 region may modify hippocampal network oscillations *in vivo*. By recording local field potentials *in vivo* from the hippocampal CA3 region of urethane-anaesthetized mutant mice at the age of postnatal 8 weeks, we found characteristic spikes with large amplitudes (1.5–4.0 mV) (Fig. 6A). These EEG spikes were consistently observed in all 6 mutant mice, but never detected in 7 control mice. The mean firing rate of the spikes ($n=136$ from 6 mice) was 0.23±0.02 Hz and the distribution of interspike intervals showed a peak at 4.75 s (Fig. 6B).

To investigate the origin of characteristic EEG spikes, we recorded field potentials in various hippocampal regions of mutant mice using a silicon probe with 16 recording sites. Simultaneous recording of a single EEG spike event from the hippocampal CA3 region and surrounding neocortex showed that the amplitude of EEG spikes was largest in the CA3 pyramidal cell layer. EEG spikes reversed their polarity in the CA3 stratum oriens (Fig. 6C). Current source density (CSD) analysis of EEG spikes revealed a current sink in the CA3 pyramidal cell layer, with a source nearby ($n=8$ from 4 mice). Recording from the cortex and hippocampal CA1 region, spikes reversed their polarity in the CA1 stratum oriens. CSD analyses revealed a large sink in the CA1 pyramidal cell layer ($n=8$ from 4 mice). On the other hand, EEG spikes recorded from the dentate gyrus showed neither polarity reversal nor sinks in CSD maps ($n=8$ from 4 mice). These results suggest that characteristic spikes are generated in the pyramidal cell layers of the CA3 and CA1 regions, but not in the dentate gyrus.

Further analysis revealed that the frequency of MUA in the CA3 pyramidal cell layer was enormously high during spike events (Fig. 6D, center). The strong correlation between MUA and EEG spikes was observed in all 4 mutant mice. After EEG spikes, MUA in the CA3 pyramidal cell layer became silent (Fig. 6D, center). MUA in the CA1 pyramidal cell layer were also associated with EEG spikes (Fig. 6D, right) and the association was reproducibly observed in all 4 mutant mice. On the other hand, there was no

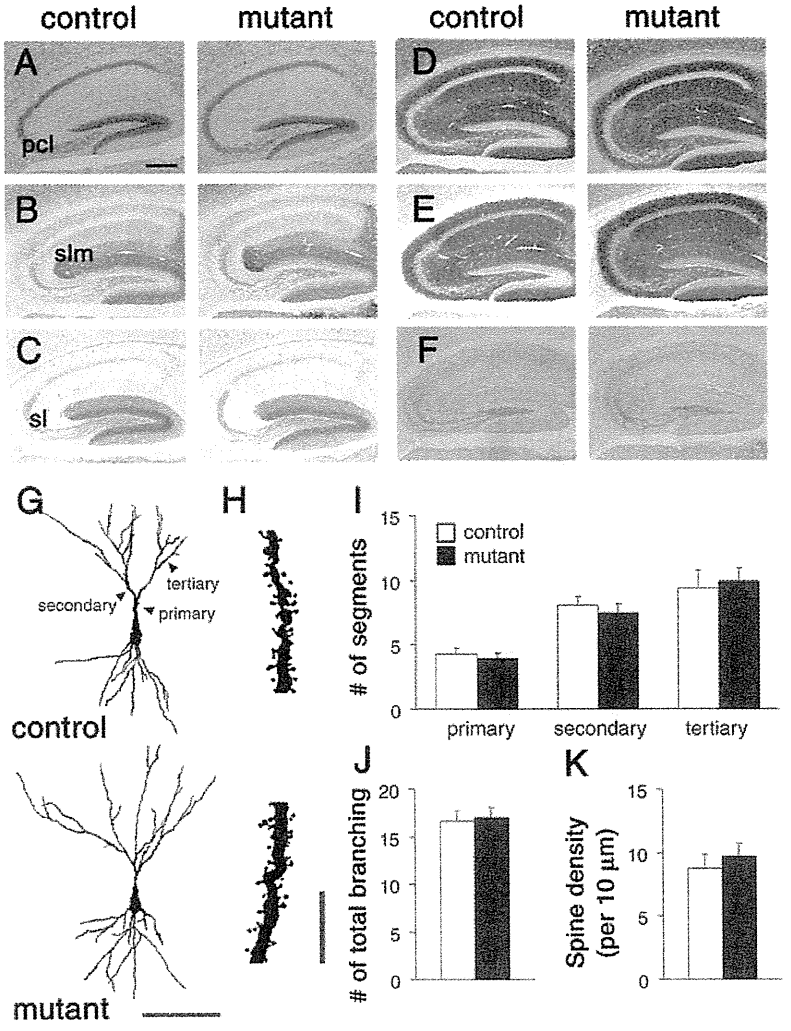

Figure 4. Normal histological organization of the hippocampal region. A, Nissl staining. **B, C**, Immunoperoxidase staining for VGluT2 (**B**) and Calbindin (**C**). **D–F**, Immunoperoxidase staining for PSD-95 (**D**), GluRα1 (**E**), and GAD (**F**). **G**, Cytoarchitecture of Golgi-stained CA3 pyramidal neurons. **H**, Higher magnification of the basal dendritic segment of CA3 pyramidal neuron in (**G**). **I–K**, Graphs represents the number of primary, secondary and tertiary dendrites (**I**), total number of dendritic branching (**J**), and spine density (**K**) of CA3 pyramidal neurons. Scale bars: **A**, 200 μm; **G**, 100 μm; **I**, 10 μm. Abbreviations: pcl, pyramidal cell layer; sl, stratum lucidum; slm, stratum lacunosum-moleculare.
doi:10.1371/journal.pone.0003993.g004

significant association in the dentate gyrus between MUA and spikes (Fig. 6D, left). The strong association of MUA with EEG spikes in the CA1 and CA3 pyramidal cell layers, but not in the dentate gyrus, together with CA3 pyramidal neuron-selective ablation of NMDA receptors, suggests that characteristic EEG spikes were originated from synchronous firing of CA3 pyramidal neurons and the activity of the CA3 network propagated to the downstream CA1 region.

Balanced excitatory and inhibitory synaptic transmission

Because either enhanced excitation or reduced inhibition can increase the excitability of hippocampal CA3 network, we examined the mRNA levels of excitatory glutamate receptor (GluR) subunits and glutamic acid decarboxylases (GADs) expressed in the hippocampal CA3 region of the mutant mice by *in situ* hybridization (Fig. 7A, Table 1). The *GluRζ1* mRNA was strongly diminished as described above. The reduction of the *GluRγ1* mRNA can be ascribed to the insertion of *cre* into one allele of the *GluRγ1* gene but the *cre* insertion exerted little effect on the kainate-induced seizure susceptibility as described above. There was no significant difference in the *GAD65* mRNA ($P=0.08$), while the level of *GAD67* mRNA was slightly but significantly reduced in the mutant mice ($P<0.001$). There were no significant differences in hybridization signals of other GluR mRNAs between control and mutant mice.

Basic electrophysiological properties of CA3 pyramidal cells were indistinguishable between two genotypes (resting membrane potential: control, -72.5 ± 0.8 mV, $n=32$; mutant -73.7 ± 1.0 mV, $n=26$, $P=0.37$; input resistance: control, 113.2 ± 5.3 MΩ; mutant, 117.7 ± 7.2 MΩ, $P=0.62$; membrane capacitance: control, 251.8 ± 9.4 pF; mutant, 250.2 ± 8.0 pF, $P=0.90$). We then compared $GABA_A$-IPSCs in the hippocampal CA3 region, which have been shown to suppress the excitability of the pyramidal cell through postsynaptic inhibition [39]. AMPA-EPSCs were evoked at −80 mV by stimulating afferent fibers in the CA3 stratum radiatum, which should activate both associa-

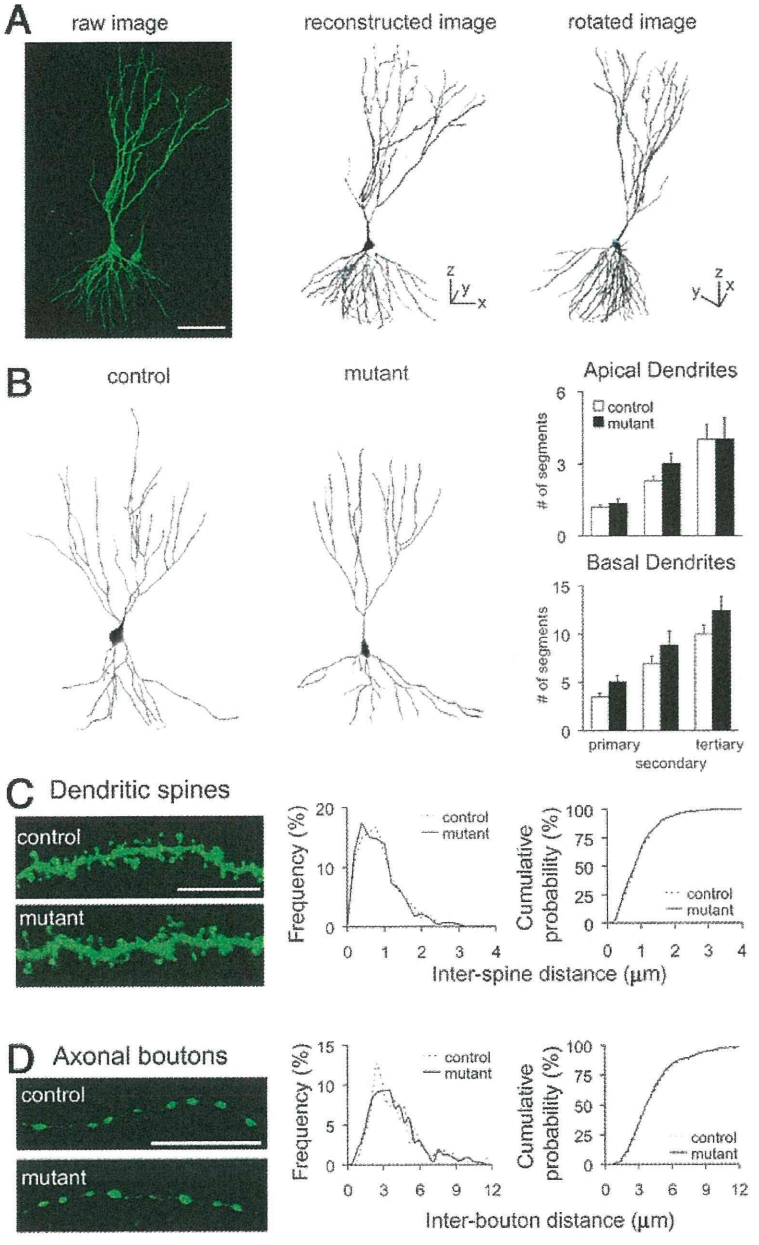

Figure 5. Dendritic branching and distribution of postsynaptic spines and presynaptic boutons in CA3 pyramidal neurons of control and mutant mice. A, Examples of three-dimensional reconstruction using IMARIS and FilamentTracer software. **B**, Three-dimensional reconstruction of AAV-EGFP-infected CA3 pyramidal neurons. Graphs represent the numbers of primary, secondary and tertiary dendrites of CA3 pyramidal neurons in control (open boxes, $n = 10–12$) and mutant mice (filled boxes, $n = 6–7$). There were no significant differences between control and mutant mice in the numbers of primary (apical, $P = 0.58$; basal, $P = 0.06$; t-test), secondary ($P = 0.13$, $P = 0.21$) and tertiary dendrites ($P = 1.0$ $P = 0.16$). **C**, Tertiary dendritic segments in control (left, top) and mutant (left, bottom) mice. Normalized distribution of inter-spine distances (middle, bin size, 0.1 μm). Cumulative distribution of inter-spine distances (right, same data set). There were no significant differences in inter-spine intervals of CA3 pyramidal neurons between two genotypes (control $n = 428$ from 10 dendrites of 4 mice; mutant, $n = 459$ from 9 dendrites of 4 mice; $P = 0.74$, Kolmogorov-Smirnov test). **D**, Boutons on the axon in the CA3 stratum radiatum of control (left, top) and mutant (left, bottom) mice. Normalized distribution of inter-bouton distances (middle, bin size, 0.4 μm). Cumulative distribution of inter-bouton distances (right, same data set). There were no significant differences in inter-bouton intervals of CA3 pyramidal neurons between two genotypes (control $n = 262$ from 18 axons of 4 mice; mutant, $n = 322$ from 24 dendrites of 4 mice; $P = 0.90$, Kolmogorov-Smirnov test).
doi:10.1371/journal.pone.0003993.g005

tional/commissural fibers and inhibitory interneurons (and their dendrites and axons), and then $GABA_A$-IPSCs were measured with the same stimulus strength at 0 mV in the presence of both the non-NMDA receptor antagonist CNQX and the NMDA receptor antagonist D-APV. The ratio of $GABA_A$-IPSCs to AMPA-EPSCs was indistinguishable between the two genotypes